# Propagation of material and surface profile uncertainties on MEMS micro-resonators using a stochastic second-order computational multi-scale approach

V. Lucas[1], J.-C. Golinval[1], R. C. Voicu[2], M. Danila[2], R. Gravila[2], R. Müller[2], A. Dinescu[2], L. Noels[1]*and L. Wu[1]

[1]*University of Liege, Department of Aeronautics and Mechanical Engineering*

*Allée de la découverte 9, B-4000 Liège, Belgium*

[2]*National Institute for R& D in Microtechnologies - IMT Bucharest*

*126A, Erou Iancu Nicolae street, 077190, Bucharest, Romania*

SUMMARY

This paper aims at accounting for the uncertainties due to material structure and surface topology of micro-beams in a stochastic multiscale model. For micro-resonators made of anisotropic polycrystalline materials, micro-scale uncertainties are due to the grain size, grain orientation, and to the surface profile. First, micro-scale realizations of stochastic volume elements (SVEs) are obtained based on experimental measurements. To account for the surface roughness, the SVEs are defined as a volume element having the same thickness as the MEMS, with a view to the use of a plate model at the structural scale. The uncertainties are then propagated up to an intermediate scale, the meso-scale, through a second-order homogenization procedure. From the meso-scale plate resultant material property realizations, a spatially correlated random field of the in plane, out of plane, and cross resultant material tensors can be characterized. Owing to this characterized random field, realizations of MEMS-scale problems can be defined on a plate finite element model. Samples of the macro-scale quantity of interest can then be computed by relying on a Monte-Carlo simulation procedure. As a case study, the resonance frequency of MEMS micro-beams is investigated for different uncertainty cases, such as grain preferred orientations and surface roughness effects.

INTERNATIONAL JOURNAL FOR NUMERICAL METHODS IN ENGINEERING

*Int. J. Numer. Meth. Engng* 2016; **00**:2–69
Received . . .
Published online in Wiley Online Library (wileyonlinelibrary.com). DOI: 10.1002/nme

KEY WORDS: Second-order multi-scale; Stochastic; Plate finite elements; Polycrystalline; Roughness; Resonance frequency

## 1. INTRODUCTION

Sources of uncertainties are most of the time neglected in numerical models. However they can affect the structural behavior, in which case it is important to consider them. This is why nowadays a lot of efforts is put into improving uncertainty quantification procedures. Dealing with uncertainties can be done in different ways, but this work focuses on the propagation of micro-scale material and geometrical uncertainties up to the structural response. Micro-scale material uncertainties result from spatially varying material properties. The structural behavior is thus non-deterministic as the material properties are statistically distributed over the structure. This structure can be modeled using the finite element method, in which case a full description of the material heterogeneities and of their variations is required. Using Monte-Carlo simulations on such a fine discretization to estimate the uncertainties in the structural behavior, *i.e.* performing direct Monte Carlo simulations, can however involve overwhelming computation costs as the finite element mesh should capture the micro-scale uncertainties. The purpose of this paper is to extend the stochastic multiscale method developed in [1], which involves uncertainty propagation across the scales for MEMS made of polycrystalline materials, to account for the grain size distribution, preferred grain orientations, and surface profile uncertainties of thin MEMS devices.

The Stochastic Finite Elements method, referred to as SFEM and described in [2, 3, 4], as a non exhaustive list, is a relevant tool to study uncertainty quantification at a reasonable cost. In the case of MEMS, this was illustrated by considering thermoelastic stochastic finite elements in [5]. SFEM to study the stochastic behavior of shells whose thickness and material properties are random was also used in [6]. However in those approaches, the random field used to describe the spatially varying

*Correspondence to: L. Noels, Phone: +32 4 366 48 26, Fax: +32 4 366 95 05, E-mail: L.Noels@ulg.ac.be

material properties and thickness was not obtained directly from micro-structure resolutions. Thus the recourse to SFEM approaches alone does not overcome the problem of modeling the material heterogeneities. Indeed, to be able to propagate the uncertainties from the micro-structure itself using SFEM, as the involved uncertainties are characterized by a small correlation length, the finite element size should be drastically reduced [7]. According to [8], accurate results are obtained when the finite element size is smaller than at least one half of the correlation length, which would lead to unreachable computational resources to capture the micro-scale heterogeneities uncertainties. However, this limitation can be overcome thanks to multi-scale approaches as the introduction of an intermediate scale implies a larger correlation length, and thus reduces the computation cost of the SFEM procedure [1].

Multi-scale approaches are an efficient, convenient, and elegant way to deal with complex heterogeneous materials. In such an analysis, three scales are defined, see Fig. 1(a). The micro-scale is the characteristic size of the micro-structure. A volume element made of the material of interest defines an intermediate scale: the meso-scale. With the help of an homogenization technique, meso-scale material properties can be estimated by the resolution of the boundary value problem (BVP) defined over the meso-scale volume element. Those homogenized properties can be used at the structural scale, the macro-scale. Different homogenization approaches were developed, such as the semi analytical mean-field homogenization (see [9, 10, 11]) or the purely numerical $FE^2$ method (see [12, 13, 14, 15, 16, 17, 18]) as non-exhaustive lists.

One of the main assumption behind computational homogenization is the scale separation which can be expressed as:

$$l_{\text{meso}} << l_{\text{macro}}, \text{ and} \tag{1}$$

$$l_{\text{micro}} << l_{\text{meso}} \, . \tag{2}$$

When dealing with reduced size structures, the characteristic size of the micro-scale heterogeneities can be too close to the macro-scale to respect both of these equations. The first one, Eq. (1), guarantees the accuracy of the procedure: accurate results are obtained when the homogenization is applied on meso-scale volume elements whose size is much smaller than the characteristic length



*Prepared using* nmeauth.cls
DOI: 10.1002/nme

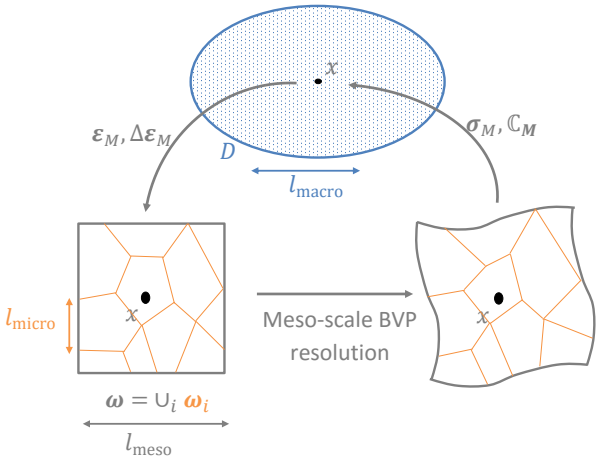


(a) 1st-order homogenization

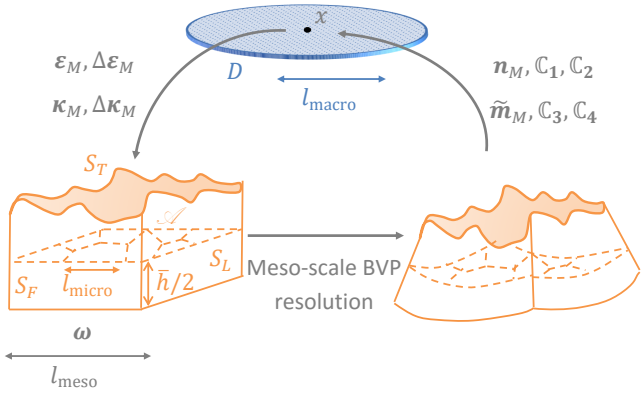


(b) 2nd-order homogenization

Figure 1. Homogenization-based multi-scale method: (a) 1st-order homogenization for classical macro-scale continuum; (b) 2nd-order homogenization for macro-scale Kirchhoff-Love plates

on which the macro-scale loading varies in space [19]. This equation should thus be satisfied but the second scale separation, Eq. (2), will thus not be respected. This implies that volume elements are not representative and they are referred to as Statistical Volume Elements (SVEs) [20]. Indeed, on the one hand, the meso-scale boundary value problem over a SVE is Boundary Condition (BC) dependent, and on the other hand, different homogenized properties are obtained for different realizations of the SVEs, even under a unique case of BCs. Although it is possible to address the lack of representativity by statistical considerations of the homogenized properties for different SVE sizes/realizations [21, 22] in order to extract mean homogenized properties or to define a



*Prepared using* nmeauth.cls
DOI: 10.1002/nme

minimum RVE size, such a method does not allow to up-scale the uncertainties. This has motivated the development of stochastic multi-scale methods.

Stochastic multi-scale analyses have been developed based on order reduction of asymptotic homogenization [23] to account for micro-scale material uncertainties in the form of random variables –and random fields in particular cases. However, accounting for general fine-scale random fields would require the nested resolution of meso-scale problems during the structural-scale analysis, leading to a prohibitive cost. Local effects can also be treated using Monte-Carlo simulations: the brittle failure of MEMS made of a poly-silicon material was studied by considering several realization of a critical zone [24] on which the relevant loading was applied. An alternative to these approaches is to introduce in the stochastic multi-scale method a meso-scale random field, obtained from a stochastic homogenization, which is in turn used as material input by the stochastic finite element method at the structural scale. In order to ensure objectivity, the size of the (structural scale) stochastic finite elements should be small enough with respect to the (spatial) correlation length of the meso-scale random field [8], the latter depending on the size of the SVEs.

In order to define a meso-scale random field, statistics and homogenization were coupled to investigate the probability convergence criterion of RVE for masonry [25], to obtain the property variations due to the grain structure of poly-silicon film [26], to extract the stochastic properties of the parameters of a meso-scale porous steel alloy material model [27], to evaluate open foams meso-scale properties [28], to extract probabilistic meso-scale cohesive laws for poly-silicon [29], to extract effective properties of random two-phase composites [30], to study the scale-dependency of homogenization for matrix-inclusion composites [31, 32], or again to consider the problem of composite materials under finite strains [33]. In this last reference, a particular attention was drawn on the correlation between the different sources of uncertainty. In most of the previously cited works, the stochastic homogenization on the SVEs was mainly achieved by a combination of computational homogenization with Monte Carlo simulations. In the recent work [34], the stochastic homogenization was achieved by using a modified version of the SFEM (here applied on the



*Prepared using* nmeauth.cls
DOI: 10.1002/nme

meso-scale boundary value problem), leading to a more efficient resolution. The problem of high-dimensionality was investigated in [35], in which the resolution of composite material elementary cells was used to explicitly define a meso-scale potential with the aim of studying the uncertainties in the fibers geometry/distribution in the case of finite elasticity of composite materials.

The meso-scale uncertainties can then be up-scaled to study the probabilistic macro-scale behavior. Based on their stochastic properties identification of the meso-scale porous steel alloy material model [27], Yin *et al.* [36] have generated a random field based on Karhunen-Loève expansion to study the macro-scale behavior. A similar approach was applied to study the dynamic behavior of open-foamed structures [28].

Recently, in order to predict relevant and consistent probabilistic macro-scale behaviors, the authors have developed in [1] a stochastic 3-scale method in the frame of MEMS vibrating beams, with a particular emphasis put on the link between the meso-scale volume element size and the macro-scale mesh size. In this approach, (i) at the micro-scale several SVEs with random grain orientations were considered; (ii) at the meso-scale, finite-element simulations on different SVEs, defined from a larger material sample by using the moving-window technique, led to the distribution of the homogenized polycrystalline material Young's modulus and of its spatial correlation; (iii) a random field of the meso-scale elastic Young's modulus was generated based on the information obtained from the SVE simulations; and (iv) the generated meso-scale random fields were used with the stochastic 1D beam finite element method to predict the statistical distribution of MEMS resonator eigen-frequencies. In particular, by comparison with direct Monte-Carlo simulations, it was shown that the generation of a spatially correlated random field allows predicting macro-scale statistical distributions independent on the SVE and macro-scale mesh sizes, as long as the distance between the macro-scale integration points remains lower than the correlation length of the meso-scale random field. This stochastic 3-scale procedure was recently extended in the frame of thermo-mechanics in [37] to study the thermo-elastic damping effect in a probabilistic way.

The purpose of this work is to develop a stochastic 3-scale method for thin polycrystalline structures able to account for the uncertainties resulting from the material heterogeneities, such



*Prepared using* nmeauth.cls
DOI: 10.1002/nme

as the grain size distributions and the preferred grain orientations, but also from the surface profile of the thin MEMS structures for which the surface roughness can be of comparable size as the MEMS thickness. Toward this end, we consider in this paper (i) a definition of the micro-structure uncertainties based on measurements on real MEMS structures, (ii) a second-order stochastic homogenization method to define statistical homogenized properties from the micro-scale information, (iii) the definition of a stochastic model able to generate meso-scale random field realizations, and (iv) plate stochastic finite elements to capture the probabilistic structural behavior.

The first step considers actual measurements on poly-silicon samples, processed at different manufacturing temperatures by Low Pressure Vapor Chemical Deposition (LPCVD), to define the uncertainties of the micro-structure. The thin structure being made of an anisotropic polycrystalline material, *i.e.* poly-silicon, the randomness in the grain size distribution and in their orientation –with or without preferred orientations– induce uncertainties. The grain size distribution is studied based on Scanning Electron Microscope (SEM) images while the distribution of orientations is obtained using X-Ray Diffraction (XRD) measurements. Another source of scatter is the surface profile of the thin structure as its roughness is of comparable size to the structure thickness. The surface topology is obtained from Atomic Force Microscopy (AFM) measurements. Both the roughness and the grain structure are correlated as it is noted in [38].

To achieve the second step of the method, *i.e.* to propagate the uncertainties due to the material structure and surface profile, a second-order homogenization procedure is considered to study the meso-scale behavior of the different (Rough) Statistical Volume Elements ((R)SVEs). With a view toward macro-scale plate simulations, second-order homogenization allows capturing the roughness effect on the bending behavior of the meso-scale volume element as it provides a bridge, not only between the in-plane stress and the in-plane strain, but also between the higher-order stress –*i.e.* bending moment– and the higher-order strain –*i.e.* curvature– as illustrated in Fig. 1(b). Second-order homogenization was described for small strains in [39, 18], and for finite strains in [40]. The method was adapted for shells in [41] or again in [42], where it was applied to study the buckling of heterogeneous shells. Owing to the second-order computational homogenization process, the



*Prepared using* nmeauth.cls
DOI: 10.1002/nme

stochastic meso-scale information, *i.e.* the shell-like resultant membrane, bending, and coupled material tensors, see Fig. 1(b), are then gathered following a simple Monte-Carlo scheme applied on (R)SVEs realizations. To obtain the spatial correlation between neighboring (R)SVEs, a moving-window technique [43] is used, thus estimating a discrete correlation function of the (R)SVEs properties. The cross-correlation between the different meso-scale properties is thus also evaluated. Indeed, as stated in [6], the influence of the cross-correlation between the Young's modulus and the Poisson ratio on the response variability is negligible in case of a static problem but this assumption is not valid when a dynamic problem is involved.

Once the stochastic behavior of the meso-scale (R)SVEs is evaluated using a sufficient number of realizations, a random field can be defined, which is the third step of the method. The two main approaches usually considered to build a random field are the Karhunen-Loève expansion, which was used in the recent work [44] for example, and the spectral representation method which was developed in [45, 46]. The latter procedure allows computing the discrete spectral density from the discrete correlation function evaluated by the stochastic homogenization using Fast Fourier Transforms and is therefore chosen in this work. The spectral representation generates Gaussian fields, but non-Gaussian fields can be retrieved through an appropriate mapping technique [47, 48, 49]. As the non-linear mapping from Gaussian to non-Gaussian changes the spectral density, an iterative procedure is required in order to obtain both the desired spectral density and non-Gaussian probability distribution. Moreover, in order to ensure the existence of the expectation of the norm of the inverse of the material tensors, a lower bound is introduced during the generation process [50].

Owing to the possibility of generating random fields, the fourth step can be performed, *i.e.* the uncertainties at the meso-scale can be propagated up to the macro-scale, in an efficient way. To take into account most of the available information at the meso-scale, such as the resultant bending material tensor, Kirchhoff-Love plate elements are considered in this work. In particular, the plate elements are formulated using a displacement-only discretization by recourse to a Discontinuous Galerkin method [51, 52]. Finally a Monte-Carlo procedure is applied: from samples of the



*Prepared using* nmeauth.cls
DOI: 10.1002/nme

meso-scale random field, samples of the MEMS properties are obtained and a statistical study is performed. On the one hand, the macro-structure is discretized using computationally efficient plate elements. On the other hand, taking advantage of the correlation length of the meso-scale random field, which is larger than the micro-structure, the macro-scale finite elements have a size which covers several heterogeneities. As a result, the macro-scale simulations involve a much lower cost compared to the direct simulations, in which the heterogeneities are explicitly discretized. Therefore the stochastic multi-scale method can be used to study the effect of the different sources of uncertainties such as grain sizes distribution, preferred grain orientations, or again surface profile, which depend on the temperature used during the Low Pressure Chemical Vapor Deposition (LPCVD) process, for different MEMS resonator geometries.

The organization of the paper is as follows. First, the stochastic finite element approach is introduced in Section 2 in the scope of plate elements. Then, the stochastic second-order homogenization and the extraction of the shell-like resultant membrane, bending, and coupled material tensors, see Fig. 1(b), are described in Section 3. Afterwards, Section 4 defines the meso-scale random field acting as a bridge between the micro to meso homogenization and the meso to macro stochastic analyzes. The method being fully introduced, Section 5 illustrates its application on a poly-silicon resonator and is subdivided into 6 subsections: Section 5.1 describes the experimental measurements; Section 5.2 deals with the generation of the (R)SVEs based on experimental measurements (SEM, XRD, AFM); Section 5.3 illustrates the extracted meso-scale statistical results; Section 5.4 compares those extracted meso-scale results to the generated meso-scale random fields; Section 5.5 studies the effect of the different uncertainties on the MEMS eigen-frequencies; and Section 5.6 reports the computational costs of the stochastic multi-scale method. Finally conclusions are drawn in Section 6.



*Prepared using* nmeauth.cls
DOI: 10.1002/nme

## 2. MACRO-SCALE PLATE SFEM

The estimation of the probability density function of the resonance frequency of a thin MEMS subjected to uncertainties is the objective of this work. The deterministic problem of an un-damped mechanical structure discretized with the finite element method can be written as

$$\boldsymbol{M}\ddot{\boldsymbol{u}} + \boldsymbol{K}\boldsymbol{u} = \boldsymbol{f}\,, \tag{3}$$

where $\boldsymbol{M}$ and $\boldsymbol{K}$ are respectively the mass and stiffness matrices, $\boldsymbol{f}$ is the assembled external force vector, and $\boldsymbol{u}$ is the assembled vector of the degrees of freedom.

The non-deterministic problem is defined on 2 different domains. The first one is the spatial domain $\boldsymbol{D}$, which is a function of the spatial coordinate $\boldsymbol{x}$. The second domain of interest is the stochastic space $\boldsymbol{\Omega}$ where $\boldsymbol{\theta} \in \boldsymbol{\Omega}$ denotes the elements in the sample space involving random quantities. To solve a non-deterministic problem defined over these 2 domains, the SFEM approach is used. As recalled in [4], a SFEM analysis can be defined by the following steps: (i) the discretization of the stochastic fields representing the properties with uncertainties; (ii) the formulation of the stochastic matrices; and (iii) the response variability calculation.

### *2.1. The random fields discretization*

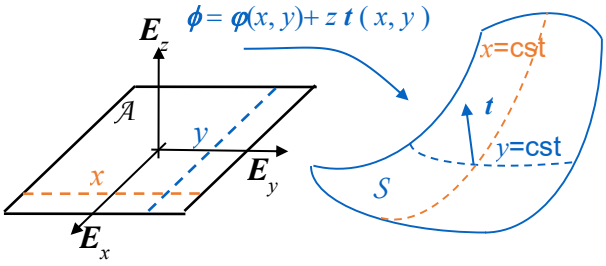


Figure 2. Representation of the plate discretization in a Cosserat plane $\mathcal{A}$ and along the thickness direction $\boldsymbol{E}_z$

For the first step, *i.e* the discretization of the stochastic field representing the uncertainties, the properties exhibiting uncertainties must be identified. One source of uncertainty is material



*Prepared using* nmeauth.cls
DOI: 10.1002/nme

related such as the grain sizes and grain orientations for polycrystalline materials. Another source comes from the geometry, such as the surface roughness. To account for both sources, we use a resultant stress-strain relation formulated for thin structures in a stochastic way. Toward this end, in this work we consider the plate representation illustrated in Fig. 2. The domain $\boldsymbol{D}$ of the plate is discretized in a Cosserat plane $\mathcal{A}$, assumed to be lying in the plane associated with the frame $(0;\ \boldsymbol{E}_x;\ \boldsymbol{E}_y)$ for simplicity, and along the thickness direction along $\boldsymbol{E}_z$. The deformation mapping $\boldsymbol{\phi}$ maps the neutral surface, represented by the Cosserat plane $\mathcal{A}$, to the deformed neutral-surface $\mathcal{S}$, and the thickness direction to the deformed unit direction $\boldsymbol{t}$, see Fig. 2. The displacement of the neutral surface is denoted by $\boldsymbol{u}$, and the change of the unit out-of-plane direction $\boldsymbol{t}$ by $\boldsymbol{\Delta t}$. In small deformations, considering Reissner-Mindlin plates, one can extract from those displacement fields, the kinematic membrane field $\boldsymbol{\varepsilon}^*$, the bending field $\boldsymbol{\kappa}^*$, and the out-of-plane shearing field $\boldsymbol{\gamma}^*$, following respectively

$$\boldsymbol{\varepsilon}^*_{\alpha\beta} = \frac{1}{2}\left(\boldsymbol{u}_{\alpha,\beta} + \boldsymbol{u}_{\beta,\alpha}\right), \tag{4}$$

$$\boldsymbol{\kappa}^*_{\alpha\beta} = \frac{1}{2}\left(\boldsymbol{\Delta t}_{\alpha,\beta} + \boldsymbol{\Delta t}_{\beta,\alpha}\right), \text{ and} \tag{5}$$

$$\boldsymbol{\gamma}^*_{\alpha} = \boldsymbol{u}_{z,\alpha} + \boldsymbol{\Delta t}_{\alpha}, \tag{6}$$

where $\alpha = x, y$ and $\beta = x, y$ correspond to the in-plane directions, and where the notation $a_{,i}$ denotes the derivatives of $a$ with respect to direction $i$.

These kinematic fields are related to the resultant membrane stresses $\boldsymbol{n}^*$,[†]

$$\boldsymbol{n}^{*\alpha} = \tilde{\boldsymbol{n}}^{*\alpha\beta}\boldsymbol{E}_\beta + \tilde{\boldsymbol{q}}^{*\alpha}\boldsymbol{E}_z, \tag{7}$$

to the resultant bending stresses $\tilde{\boldsymbol{m}}^*$,

$$\tilde{\boldsymbol{m}}^{*\alpha} = \tilde{\boldsymbol{m}}^{*\alpha\beta}\boldsymbol{E}_\beta, \tag{8}$$

and to the shear resultant stresses $\boldsymbol{n}^{*z}$

$$\boldsymbol{n}^{*z} = \tilde{\boldsymbol{q}}^{*\alpha}\boldsymbol{E}_\alpha. \tag{9}$$

[†]All along this section we use the classical notations for plates and shells described in a non-orthonormal referential with superscripts for stress related fields, although in this paper the basis remains orthonormal. Similarly, we use the ˜ notation to refer to the uncoupled in-plane/out-of-plane components, although for plates they are naturally uncoupled.



*Prepared using* nmeauth.cls
DOI: 10.1002/nme

The different components of those vectors result from the integration of the stress tensor over the thickness $h$, with

$$\tilde{\boldsymbol{n}}^{*\alpha\beta} = \int_h \boldsymbol{\sigma}^{\alpha\beta} dz, \tag{10}$$

$$\tilde{\boldsymbol{m}}^{*\alpha\beta} = \int_h \boldsymbol{\sigma}^{\alpha\beta} z dz, \text{ and} \tag{11}$$

$$\tilde{\boldsymbol{q}}^{*\alpha} = \int_h \boldsymbol{\sigma}^{\alpha z} dz. \tag{12}$$

In elasticity, the linear relationships between the resultant kinematic fields and the resultant stresses can be expressed as

$$\tilde{\boldsymbol{n}}^* = \mathbb{C}_1^* : \boldsymbol{\varepsilon}^* + \mathbb{C}_2^* : \boldsymbol{\kappa}^* + \mathbb{C}_5^* \cdot \boldsymbol{\gamma}^*, \tag{13}$$

$$\tilde{\boldsymbol{m}}^* = \mathbb{C}_3^* : \boldsymbol{\varepsilon}^* + \mathbb{C}_4^* : \boldsymbol{\kappa}^* + \mathbb{C}_6^* \cdot \boldsymbol{\gamma}^*, \tag{14}$$

$$\tilde{\boldsymbol{q}}^* = \mathbb{C}_7^* : \boldsymbol{\varepsilon}^* + \mathbb{C}_8^* : \boldsymbol{\kappa}^* + \mathbb{C}_9^* \cdot \boldsymbol{\gamma}^*, \tag{15}$$

with, in all generalities the fourth-order tensors $\mathbb{C}_1^*$, $\mathbb{C}_2^*$, $\mathbb{C}_3^*$, and $\mathbb{C}_4^*$ in $\mathbb{R}^4$, the third-order tensors $\mathbb{C}_5^*$, $\mathbb{C}_6^*$, $\mathbb{C}_7^*$, and $\mathbb{C}_8^*$ in $\mathbb{R}^3$, and the second-order tensor $\mathbb{C}_9^*$ in $\mathbb{R}^2$.

In this paper we will consider the Kirchhoff-Love plate theory, which implies that $\boldsymbol{\Delta t}_\alpha = -\boldsymbol{u}_{z,\alpha}$, $\boldsymbol{\kappa}_{\alpha\beta}^* = -\boldsymbol{u}_{z,\alpha\beta}$, and $\tilde{\boldsymbol{q}}^{*\alpha} = 0$. In other words, the section of the plate remains perpendicular to the membrane after deformation. As a result, the set of Eqs. (13-15) simplifies into

$$\tilde{\boldsymbol{n}}^* = \mathbb{C}_1^* : \boldsymbol{\varepsilon}^* + \mathbb{C}_2^* : \boldsymbol{\kappa}^*, \tag{16}$$

$$\tilde{\boldsymbol{m}}^* = \mathbb{C}_3^* : \boldsymbol{\varepsilon}^* + \mathbb{C}_4^* : \boldsymbol{\kappa}^*. \tag{17}$$

Those last expressions can be rewritten under the matrix form

$$\boldsymbol{\psi}_\sigma^\star = \boldsymbol{U}(\boldsymbol{x}, \boldsymbol{\theta}) \boldsymbol{\chi}_\varepsilon^\star, \tag{18}$$

where $\boldsymbol{\chi}_\varepsilon^\star$ corresponds to the resultant kinematic fields ordered in a vector notation and $\boldsymbol{\psi}_\sigma^\star$ corresponds to the resultant stresses ordered in a vector notation. The corresponding resultant material operator $\boldsymbol{U}(\boldsymbol{x}, \boldsymbol{\theta})$ defines the shell-like material behavior at a spatial position $\boldsymbol{x}$ for a sample $\boldsymbol{\theta}$. In this paper, the resultant material operator is computed through a multi-scale procedure: a volume element is associated to each position $\boldsymbol{x}$ for a sample $\boldsymbol{\theta}$ thus forming a boundary value



*Prepared using* nmeauth.cls
DOI: 10.1002/nme

problem (BVP). As small scale volume elements are considered, they are not representative and therefore referred to as SVE or Statistical Volume Elements. The resolution of the stochastic BVP determines $\boldsymbol{U}(\boldsymbol{x},\boldsymbol{\theta})$. A random field is thus defined so that $\boldsymbol{U}(\boldsymbol{x},\boldsymbol{\theta}) : \mathcal{A}\times\boldsymbol{\Omega}\rightarrow\boldsymbol{M}_N^{+s}(\mathbb{R})$ where $\boldsymbol{M}_N^{+s}(\mathbb{R})$ refers to the set of all symmetric positive-definite real matrices of size $N\times N$. The demonstration that $\boldsymbol{U}\in\boldsymbol{M}_N^{+s}(\mathbb{R})$ is reported in Appendix A.

Besides the material uncertainties, the influence of the roughness is also studied. Rough SVEs are referred to as RSVEs. When both cases, rough or flat, are possible, the volume elements are referred to as (R)SVEs. The roughness has effects on the mechanical behavior of the volume element, thus affecting $\boldsymbol{U}(\boldsymbol{x},\boldsymbol{\theta})$. It also affects the distribution of mass over the macro-scale structure and thus another random field must be defined. Therefore the mass per membrane unit area random field $\bar{\rho}(\boldsymbol{x},\boldsymbol{\theta}) : \mathcal{A}\times\boldsymbol{\Omega}\rightarrow\mathbb{R}^+$ is now introduced as it is commonly done for plate elements. Note that plate elements also involve the cross section inertia $I_p$. However the contribution to the mass matrix of this last term being much smaller than the contribution from $\bar{\rho}$ (the ratio between the two being of the order of $h/l_{\text{macro}}$), we actually approximate the uncertainty effect in $I_p$ by approximating the term as $I_p = \frac{\bar{\rho}^3}{12\rho^2}$.

In order to evaluate the random fields, the point discretization method is considered in this work. At each integration point $\boldsymbol{x}^i$ of the plate finite elements, the random fields are evaluated thus leading to the mass per membrane unit area $\bar{\rho}(\boldsymbol{x}^i,\boldsymbol{\theta})$ and the resultant material operator $\boldsymbol{U}(\boldsymbol{x}^i,\boldsymbol{\theta})$. Note that the point discretization method is easy to implement but it tends to over-represent the uncertainties in each element [53]. The mesh elements must thus be small enough compared to the correlation length of the random field so that the properties can be considered constant over the mesh element part related to an integration point. As we are dealing with linear plate elements, the computational time of the SFEM remains affordable, which justifies this discretization method choice. However, other discretization methods, such as the local average method, exist [53] and could be considered for more complex structural simulations.



*Prepared using* nmeauth.cls
DOI: 10.1002/nme

*2.2. The formulation of the stochastic matrices*

The second step is the formulation of the stochastic matrices which define the problem: the mass and the stiffness matrix. They must be defined from the governing equations which are, for a thin body $\boldsymbol{D}$, the equilibrium of forces and moments, respectively

$$\rho\ddot{\boldsymbol{u}} = \boldsymbol{b} + \boldsymbol{\nabla}\cdot\boldsymbol{\sigma} \quad \text{in } \boldsymbol{D}, \text{ and} \tag{19}$$

$$\boldsymbol{\phi}\wedge\rho\ddot{\boldsymbol{u}} = \boldsymbol{\phi}\wedge\boldsymbol{b} + \boldsymbol{\phi}\wedge\boldsymbol{\nabla}\cdot\boldsymbol{\sigma} \quad \text{in } \boldsymbol{D}, \tag{20}$$

where $\boldsymbol{b}$ represents the external forces and $\boldsymbol{\phi}$ is the position mapping. The input values of this mapping are the Cosserat plane $\mathcal{A}$ coordinates of the thin body and the coordinate along the normalized thickness. The output of the mapping is the actual current configuration. The main idea behind plate elements is to avoid the discretization along the thickness direction by considering the thin body assumption. Therefore the governing equations for plates are obtained after integration of Eqs. (19) and (20) over the thickness, which results in the strong form of the Reissner-Mindlin plates, respectively

$$\bar{\rho}\ddot{\boldsymbol{u}} = \boldsymbol{n}^{*\alpha}_{,\alpha} + \bar{\boldsymbol{n}} \quad \text{in } \mathcal{A}, \text{ and} \tag{21}$$

$$I_p\ddot{\boldsymbol{t}} = \bar{\tilde{\boldsymbol{m}}} - (\boldsymbol{n}^{*z} - \lambda\boldsymbol{E}_z) + \tilde{\boldsymbol{m}}^{*\alpha}_{,\alpha} \quad \text{in } \mathcal{A}, \tag{22}$$

where $I_p$ is the mass inertia per unit width, $\boldsymbol{t}$ is the direction of the membrane plane, $\lambda$ is an undefined pressure applied along the thickness direction, and $\bar{\boldsymbol{n}}$ and $\bar{\tilde{\boldsymbol{m}}}$ are respectively the resultant external surface traction per unit length and the resultant external torque per unit length.

As previously stated, the Kirchhoff-Love plate theory is considered. Furthermore, small deformations/rotations and plane-stress state are assumed. The Cosserat plane $\mathcal{A}$ of the plate can be divided into finite elements $\mathcal{A}^e$, such that $\mathcal{A} = \bigcup_e \mathcal{A}^e$. Under these assumptions, the weak form corresponding to the set of Eqs. (21-22) is obtained by multiplying the equations (21-22) by respectively $\delta\boldsymbol{u}$ and $-\delta\boldsymbol{u}_{z,\alpha}\boldsymbol{E}_\alpha$, by integrating on the sum of the elements $\mathcal{A}^e$, by adding the two virtual energies and isolating the virtual contributions in the Cosserat plane ($\delta\boldsymbol{u}_\alpha$) and along the out-of-plane direction ($\delta\boldsymbol{u}_z$), by integrating by parts on each element $\mathcal{A}^e$, and by applying the Gauss



*Prepared using* nmeauth.cls DOI: 10.1002/nme

theorem [54]. Omitting the external forces contributions for conciseness, this results into

$$\sum_e \int_{\mathcal{A}^e} \bar{\rho}\ddot{\boldsymbol{u}}_\alpha \delta\boldsymbol{u}_\alpha d\mathcal{A}^e \quad + \quad \sum_e \int_{\mathcal{A}^e} \tilde{\boldsymbol{n}}^{*\alpha\beta} \delta\boldsymbol{u}_{\beta,\alpha} d\mathcal{A}^e \quad = \quad \sum_e \int_{\partial\mathcal{A}^e} \tilde{\boldsymbol{n}}^{*\alpha\beta} \delta\boldsymbol{u}_\beta \boldsymbol{\nu}_\alpha d\partial\mathcal{A}^e, \quad (23)$$

$$\sum_e \int_{\mathcal{A}^e} \bar{\rho}\ddot{\boldsymbol{u}}_z \delta\boldsymbol{u}_z d\mathcal{A}^e + \sum_e \int_{\mathcal{A}^e} I_p \ddot{\boldsymbol{u}}_{z,\alpha} \delta\boldsymbol{u}_{z,\alpha} d\mathcal{A}^e + \sum_e \int_{\mathcal{A}^e} \left(-\tilde{\boldsymbol{m}}^{*\alpha\beta} \delta\boldsymbol{u}_{z,\alpha\beta}\right) d\mathcal{A}^e = \sum_e \int_{\partial\mathcal{A}^e} \left(-\tilde{\boldsymbol{m}}^{*\alpha\beta} \delta\boldsymbol{u}_{z,\beta}\right) \boldsymbol{\nu}_\alpha d\partial\mathcal{A}^e, \quad (24)$$

where $\boldsymbol{\nu}$ is the outward unit normal to the elements contour $\partial\mathcal{A}^e$ (in the Cosserat plane). In these expressions, we have kept the boundary contribution of each element. Indeed, those terms vanish in Eq. (23) by continuity of the kinematically admissible displacement $\delta\boldsymbol{u}_\beta$, but as the gradient $\delta\boldsymbol{u}_{z,\alpha}$ of the kinematically admissible displacement is not continuous across element interfaces, these terms have to be kept in the weak form (24). After ensuring stability and symmetrization related to the discontinuity of $\boldsymbol{u}_{z,\alpha}$, this results in a Continuous/Discontinuous Galerkin formulation of the bending equations similar to the ones developed in [51, 52][‡]:

$$\sum_e \int_{\mathcal{A}^e} \bar{\rho}\ddot{\boldsymbol{u}}_\alpha \delta\boldsymbol{u}_\alpha d\mathcal{A}^e \quad + \quad \sum_e \int_{\mathcal{A}^e} \tilde{\boldsymbol{n}}^{*\alpha\beta} \delta\boldsymbol{u}_{\beta,\alpha} d\mathcal{A}^e \quad = \quad 0, \quad (25)$$

$$\begin{aligned}\sum_e \int_{\mathcal{A}^e} \bar{\rho}\ddot{\boldsymbol{u}}_z \delta\boldsymbol{u}_z d\mathcal{A}^e + \sum_e \int_{\mathcal{A}^e} I_p \ddot{\boldsymbol{u}}_{z,\alpha} \delta\boldsymbol{u}_{z,\alpha} d\mathcal{A}^e + \sum_e \int_{\mathcal{A}^e} \left(-\tilde{\boldsymbol{m}}^{*\alpha\beta} \delta\boldsymbol{u}_{z,\alpha\beta}\right) d\mathcal{A}^e + \\ \sum_s \int_{(\partial_I\mathcal{A})^s} \left\langle \tilde{\boldsymbol{m}}^{*\alpha\beta} \right\rangle \left[\!\left[ -\delta\boldsymbol{u}_{z,\beta} \boldsymbol{\nu}_\alpha \right]\!\right] d\partial\mathcal{A}^e + \\ \sum_s \int_{(\partial_I\mathcal{A})^s} \left\langle \mathbb{C}_3^{*\alpha\beta\gamma\delta} \delta\boldsymbol{\varepsilon}^*_{\gamma\delta} + \mathbb{C}_4^{*\alpha\beta\gamma\delta} \delta\boldsymbol{\kappa}^*_{\gamma\delta} \right\rangle \left[\!\left[ -\boldsymbol{u}_{z,\beta} \boldsymbol{\nu}_\alpha \right]\!\right] d\partial\mathcal{A}^e + \\ \sum_s \int_{(\partial_I\mathcal{A})^s} \left[\!\left[ -\delta\boldsymbol{u}_{z,\beta} \boldsymbol{\nu}_\alpha \right]\!\right] \left\langle \frac{\beta_s}{h_s} \mathbb{C}_4^{*\alpha\beta\gamma\delta} \right\rangle \left[\!\left[ -\boldsymbol{u}_{z,\gamma} \boldsymbol{\nu}_\delta \right]\!\right] d\partial\mathcal{A}^e = 0, \quad (26)\end{aligned}$$

where $(\partial_I\mathcal{A})^s$ is an interface between two plate elements, $\langle\ \rangle$ is the average operator defined from the two values of the neighboring elements, $[\![\ ]\!]$ is the jump operator defined from the two values of the neighboring elements[§], $\beta_s$ is the stabilization parameter that has to be larger than a value depending

[‡]Continuous as $\boldsymbol{u}_z$ is such and discontinuous as $\boldsymbol{u}_{z,\alpha}$ is such.

[§]Considering two adjacent elements "+" and "-", the average operator of a field $\bullet$ is defined as $\langle\bullet\rangle = \frac{1}{2}(\bullet^+ + \bullet^-)$, and the jump operator of a field $\bullet$ as $[\![\bullet\boldsymbol{\nu}]\!] = (\bullet^+ - \bullet^-)\boldsymbol{\nu}^-$, where the superscript "$\pm$" refers to the field evaluated on element "$\pm$".



*Prepared using* nmeauth.cls DOI: 10.1002/nme

on the polynomial approximation only, and where $h_s$ is the mesh size. In such a framework, the problem is formulated in terms of the sole displacement field $\boldsymbol{u}$ of the Cosserat plane. We refer to [51, 52, 54] for more details.

Finally, the finite element discretization is obtained using the polynomial interpolation

$$\boldsymbol{u} = N^a \boldsymbol{u}^a \,, \tag{27}$$

where $N^a$ is the shape function at node $a$ and $\boldsymbol{u}^a$ are the nodal displacements of the Cosserat surface $\mathcal{A}$. The assembled mass and stiffness matrices can thus be computed resulting in the system of equations

$$\boldsymbol{M}^{ab}(\boldsymbol{\theta})\,\ddot{\boldsymbol{u}}^b + \boldsymbol{K}^{ab}(\boldsymbol{\theta})\,\boldsymbol{u}^b = 0\,. \tag{28}$$

### *2.3. Response variability calculation*

The third step of SFEM involves the response variability calculation. Toward this end, a Monte-Carlo simulation is used. This method is simple and efficient: samples of the quantity of interest are computed by solving different finite element realizations. Based on these resolutions, moments and probability density functions of the macro-scale response can be estimated. The drawback of Monte-Carlo simulations lies in the computational cost. If the meso-scale random field is known, the stochastic behavior of the quantity of interest can be estimated at a much lower cost with the perturbation technique for example, as described in [2], but this is not as accurate as MC approaches. However, the multi-scale approach leads to an important computational cost reduction so that Monte-Carlo simulations remain affordable.

## 3. SECOND ORDER HOMOGENIZATION IN THE FRAME OF PLATE ELEMENTS

In this section, the meso-scale material properties $\boldsymbol{U}(\boldsymbol{x},\boldsymbol{\theta})$, see Eq. (18), which corresponds to the 4 resultant material tensors $\mathbb{C}_1^* - \mathbb{C}_4^*$ written under the matrix form, are extracted from the meso-scale volume element BVP resolution. The meso-scale RSVE $\omega$ is almost a parallelepiped, with 5 flat surfaces and 1 rough surface when roughness is considered, see Fig. 1(b). Each surface is referred



*Prepared using* nmeauth.cls DOI: 10.1002/nme

to as either $S_F$, $S_{BA}$, $S_L$, $S_R$, $S_T$, or $S_{BO}$ respectively for the forward, backward, left, right, top and bottom surfaces, the top surface being the one which might be rough. The average plane of the rough surface defines the thickness $\bar{h}$ of the RSVE.

In the first part of this section, generalities about second-order computational homogenization are recalled. In particular, the second-order homogenization process for thin structures is described. Afterwards, consistent boundary conditions on rough volume elements are defined. Finally, from the homogenization process, the matrix $\boldsymbol{U}$ is extracted in order to contain all the information required for the macro-scale plate elements resolution under the Kirchhoff-Love assumption, *i.e.* the resultant material tensors $\mathbb{C}_1^* - \mathbb{C}_4^*$.

### *3.1. Second-order homogenization*

In the context of a first-order computational homogenization, the only kinematic constraint is first order [19]. Assuming small deformations, the symmetric macro-scale Cauchy strain tensor $\boldsymbol{\varepsilon}_M$ thus drives the problem while $\boldsymbol{u}_M$ is the displacement at the macro-scale. In the following, the subscript "$M$" refers to a macro-scale quantity. Under the infinitesimal strain assumption, the Cauchy strain is linked to the displacement by:

$$\boldsymbol{\varepsilon}_M = \frac{1}{2}\left(\boldsymbol{\nabla} \otimes \boldsymbol{u}_M + (\boldsymbol{\nabla} \otimes \boldsymbol{u}_M)^T\right). \tag{29}$$

Besides, the unsymmetrical strain $\boldsymbol{\upsilon}_M$, which possibly includes the rotation of the volume element, is defined by

$$\boldsymbol{\upsilon}_M = \boldsymbol{u}_M \otimes \boldsymbol{\nabla}. \tag{30}$$

In the case of second-order homogenization, described in [40] for large deformations and in [18] for small strains, the gradient of the deformation gradient is also introduced. It is denoted $\boldsymbol{\eta}_M$ and reads

$$\boldsymbol{\eta}_M = \boldsymbol{u}_M \otimes \boldsymbol{\nabla} \otimes \boldsymbol{\nabla}. \tag{31}$$

In a deformation driven macro-scale procedure, the different stress components are computed from the macro-scale deformation state characterized by $\boldsymbol{\upsilon}_M$ and $\boldsymbol{\eta}_M$, see Fig. 1(b). The idea behind multi-scale computation is to link stress and strain through the resolution of a meso-scale boundary



*Prepared using* nmeauth.cls
DOI: 10.1002/nme

value problem. This meso-scale BVP is described by a micro-scale displacements $\boldsymbol{u}_m$, the subscript "$m$" corresponding to a micro-scale quantity. From a second order Taylor expansion applied on the macro-scale displacement, one can define the micro-scale displacement as

$$\boldsymbol{u}_m = \boldsymbol{\upsilon}_M \cdot \boldsymbol{x} + \frac{1}{2}\boldsymbol{\eta}_M : (\boldsymbol{x} \otimes \boldsymbol{x}) + \boldsymbol{u}'_m, \tag{32}$$

where $\boldsymbol{u}'_m$ is the micro-scale fluctuation field. The micro-scale Cauchy strain tensor is defined as the gradient of the micro-scale displacement, with

$$\boldsymbol{\upsilon}_m = \boldsymbol{u}_m \otimes \boldsymbol{\nabla} = \boldsymbol{\upsilon}_M + \boldsymbol{\eta}_M \cdot \boldsymbol{x} + \boldsymbol{u}'_m \otimes \boldsymbol{\nabla}. \tag{33}$$

Ensuring the strain scale-transition during the down-scaling process follows from

$$\boldsymbol{\upsilon}_M = \frac{1}{V}\int_{\omega} \boldsymbol{\upsilon}_m d\omega. \tag{34}$$

This scale transition is satisfied if the following two conditions, based on the definition of the micro-scale strain in Eq. (33), are respected:

$$\int_{\omega} \boldsymbol{x} d\omega = 0, \text{ and} \tag{35}$$

$$\int_{\omega} \boldsymbol{u}'_m \otimes \boldsymbol{\nabla} d\omega = 0. \tag{36}$$

Equation (35) is always satisfied if the volume element is centered at its centroïd. This implies that if Eq. (34) has to be satisfied, the boundary conditions should be defined accordingly to Eq. (36), which using the divergence theorem can be rewritten in terms of the surface integral as

$$\int_{\partial\omega} \boldsymbol{n} \otimes \boldsymbol{u}'_m d\partial\omega = 0, \tag{37}$$

where $\boldsymbol{n}$ is the unit vector normal to the surface $\partial\omega$ of the volume element.

Besides down-scaling the strain tensor, the higher-order strain tensor ensures a correct constraint of the high-order deformation modes. To define this down-scaling, Eq. (33) is first multiplied by the position

$$\boldsymbol{\upsilon}_m \otimes \boldsymbol{x} = (\boldsymbol{u}_m \otimes \boldsymbol{\nabla}) \otimes \boldsymbol{x} = \boldsymbol{\upsilon}_M \otimes \boldsymbol{x} + \boldsymbol{\eta}_M \cdot (\boldsymbol{x} \otimes \boldsymbol{x}) + (\boldsymbol{u}'_m \otimes \boldsymbol{\nabla}) \otimes \boldsymbol{x}. \tag{38}$$



*Prepared using* nmeauth.cls
DOI: 10.1002/nme

Integrating this last equation on the volume, using Eq. (35), defining the inertia $\boldsymbol{J} = \frac{1}{V}\int_{\omega} \boldsymbol{x} \otimes \boldsymbol{x} d\omega$, and integrating by parts the displacement and fluctuation related terms lead to

$$\frac{1}{V}\int_{\partial\omega} \boldsymbol{u}_m \otimes \boldsymbol{n} \otimes \boldsymbol{x} d\partial\omega - \frac{1}{V}\int_{\omega} \boldsymbol{u}_m d\omega \otimes \boldsymbol{I} = \boldsymbol{\eta}_M \cdot \boldsymbol{J} - \frac{1}{V}\int_{\omega} \boldsymbol{u}'_m d\omega \otimes \boldsymbol{I} + \frac{1}{V}\int_{\partial\omega} \boldsymbol{u}'_m \otimes \boldsymbol{n} \otimes \boldsymbol{x} d\partial\omega, \quad (39)$$

where $\boldsymbol{I}$ is the identity tensor. Substituting Eq. (32) in the second term of the left hand side of Eq. (39) and using Eq. (35) result into

$$\frac{1}{V}\int_{\partial\omega} \boldsymbol{u}_m \otimes \boldsymbol{n} \otimes \boldsymbol{x} d\partial\omega - \frac{1}{2}\boldsymbol{\eta}_M : \boldsymbol{J} \otimes \boldsymbol{I} = \boldsymbol{\eta}_M \cdot \boldsymbol{J} + \frac{1}{V}\int_{\partial\omega} \boldsymbol{u}'_m \otimes \boldsymbol{n} \otimes \boldsymbol{x} d\partial\omega. \quad (40)$$

From this equation, in order for the high-order strain down-scaling to be independent on the fluctuation field, the following condition should be satisfied

$$\int_{\partial\omega} \boldsymbol{u}'_m \otimes \boldsymbol{n} \otimes \boldsymbol{x} d\partial\omega = 0. \quad (41)$$

Both micro-scale and macro-scale problems are now defined as well as the kinematic scale transition. However, a multi-scale approach only provides a relevant solution when the transition between the micro- and the macro-scales is energetically consistent. This consistency is achieved by appropriate choices of the boundary conditions. Energetically consistent boundary conditions are obtained if the Hill-Mandel condition, which states the conservation of energy variation between the micro-scale and the macro-scale problems, is satisfied. From the micro-scale energy per unit area $S$ of the Cosserat plane, one can obtain[¶]:

$$\begin{aligned} \frac{1}{S}\int_{\omega} \boldsymbol{\sigma}_m : \delta\boldsymbol{\upsilon}_m d\omega &= \frac{1}{S}\int_{\omega} \boldsymbol{\sigma}_m : (\delta\boldsymbol{\upsilon}_M + \delta\boldsymbol{\eta}_M \cdot \boldsymbol{x} + \delta\boldsymbol{u}'_m \otimes \boldsymbol{\nabla}) d\omega \\ &= \boldsymbol{n}_M : \delta\boldsymbol{\varepsilon}_M + \tilde{\boldsymbol{m}}_M \vdots \delta\boldsymbol{\eta}_M + \frac{1}{S}\int_{\omega} \boldsymbol{\sigma}_m : (\delta\boldsymbol{u}'_m \otimes \boldsymbol{\nabla}) d\omega, \end{aligned} \quad (42)$$

with the force and moment per unit width

$$\boldsymbol{n}_M = \frac{1}{S}\int_{\omega} \boldsymbol{\sigma}_m d\omega, \text{ and} \quad (43)$$

$$\tilde{\boldsymbol{m}}_M = \frac{1}{S}\int_{\omega} \frac{\boldsymbol{\sigma}_m \otimes \boldsymbol{x} + (\boldsymbol{\sigma}_m \otimes \boldsymbol{x})^{rc}}{2} d\omega, \quad (44)$$

[¶]As $\boldsymbol{\sigma}$ is symmetric, $\boldsymbol{\sigma} : \delta\boldsymbol{\upsilon} = \boldsymbol{\sigma} : \delta\boldsymbol{\varepsilon} = \boldsymbol{\sigma}_{ij}\delta\boldsymbol{\varepsilon}_{ij}$.



*Prepared using* nmeauth.cls DOI: 10.1002/nme

where the superscript "*rc*" means right transposed, *i.e.* $(\boldsymbol{A}^{rc})_{ijk} = \boldsymbol{A}_{ikj}$, and the triple contraction product is defined as $\boldsymbol{A}\dddot{:}\boldsymbol{B} = \boldsymbol{A}_{ijk}\boldsymbol{B}_{ijk}$.

Equation (42) implies that the Hill-Mandel condition is fulfilled if

$$\frac{1}{S}\int_{\omega} \boldsymbol{\sigma}_m : (\delta \boldsymbol{u}'_m \otimes \boldsymbol{\nabla})\, d\omega = 0\,, \tag{45}$$

or again, using the divergence theorem, if

$$\frac{1}{S}\int_{\partial\omega} \boldsymbol{t}_m \cdot \delta \boldsymbol{u}'_m d\partial\omega = 0\,, \tag{46}$$

where $\boldsymbol{t}_m = \boldsymbol{n}\cdot\boldsymbol{\sigma}_m$ and $\boldsymbol{n}$ is the unit outward vector normal to the surface $\partial\omega$ (the surface of the meso-scale volume element $\omega$, which is not equal to $S$ the surface of the Cosserat plane).

### *3.2. Boundary conditions*

Equation (46) defines the boundary conditions of the meso-scale BVP required to satisfy the Hill-Mandel condition. Equations (37) and (41) ensure the correct down-scaling of the strain tensors.

Due to the rough top surface, the boundary condition on the (R)SVE must be applied carefully. As proposed in [41], thin structures can be considered for which the plane-stress state is assumed. The top and bottom surfaces are then stress-free with

$$\boldsymbol{t}_m(\boldsymbol{x}) = \boldsymbol{0} \qquad \forall \boldsymbol{x} \in S_T \cup S_{BO}, \tag{47}$$

which satisfies (46) on the $S_T \cup S_{BO}$ part of $\partial\omega$. The conditions (37) and (41) are not constrained on those faces, and as a result some macro-strain and higher-order macro-strain modes cannot be down-scaled on the SVE. However, this is in agreement with the plate kinematics as it will be discussed in Section 3.3.

The fluctuation field is constrained on the other four flat surfaces $S_i$. Equation (37) is automatically satisfied with Kinematic Uniform Boundary Conditions (KUBCs) $-\boldsymbol{u}'_m = 0$, Periodic Boundary Conditions (PBCs) –as $\boldsymbol{u}'_m$ are the same and the normal vectors are opposite on opposite faces, while Eq. (41) is automatically satisfied for KUBCs and also for PBCs if Zero Average Fluctuation Boundary Condition (ZAFBC) $\int_{S_i} \boldsymbol{u}'_m d\partial\omega = 0$ is enforced simultaneously on two (e.g. $S_F$ and $S_L$) of the four flat surfaces $S_i$ [56].



*Prepared using* nmeauth.cls
DOI: 10.1002/nme

In this paper we choose to apply Mixed Uniform Boundary Conditions (MUBCs). Although periodic boundary conditions could also be considered, as the geometry is not periodic MUBCs are a simpler alternative. Moreover it has been shown in [1] that the effect of the grain uncertainties is more important than the effect of the boundary conditions. In order to apply MUBCs, on the one hand, Kinematic Uniform Boundary Conditions (KUBCs) are considered in the plate in-plane directions:

$$\boldsymbol{u}'_{m_x}(\boldsymbol{x}) = \boldsymbol{u}'_{m_y}(\boldsymbol{x}) = 0 \qquad \forall \boldsymbol{x} \in S_F \cup S_{BA}, \text{ and } \forall \boldsymbol{x} \in S_L \cup S_R, \tag{48}$$

where the $x$-direction is the direction normal to the surfaces $S_F$ and $S_{BA}$, and the $y$-direction is the direction normal to the surfaces $S_L$ and $S_R$. On the other hand, Static Uniform Boundary Conditions (SUBCs) are considered in the plate out-of-plane direction, with

$$\boldsymbol{t}^z_m = \boldsymbol{n}_{m_k} \boldsymbol{\sigma}^{kz}_M \quad \forall \boldsymbol{x} \in S_F \cup S_{BA}, \text{ and } \forall \boldsymbol{x} \in S_L \cup S_R. \tag{49}$$

Combining Eqs. (48) and (49), as $S_F$ and $S_{BA}$ are opposite flat surfaces, the Hill-Mandel condition (46) can be verified for the forward and backward surfaces part of $\partial\omega$ as

$$\int_{S_F \cup S_{BA}} \boldsymbol{t}^i_m \boldsymbol{u}'_{m_i} d\partial\omega \quad = \quad \int_{S_F \cup S_{BA}} \boldsymbol{t}^z_m \boldsymbol{u}'_{m_z} d\partial\omega = \boldsymbol{\sigma}^{kz}_M \int_{S_F \cup S_{BA}} \boldsymbol{n}_{m_k} \boldsymbol{u}'_{m_z} d\partial\omega. \tag{50}$$

This last term vanishes providing the Zero Average Fluctuation Boundary Condition (ZAFBC) has also been enforced on the two surfaces for the $z$-component:

$$\int_{S_F} \boldsymbol{u}'_{m_z} d\partial\omega = \int_{S_{BA}} \boldsymbol{u}'_{m_z} d\partial\omega = 0\,. \tag{51}$$

The same applies for the last two surfaces $S_L$ and $S_R$, satisfying the Hill-Mandel condition.

For these last four side surfaces, because of Eqs. (48) and (51), Eq. (37) is also satisfied. However, although the condition (41) is automatically satisfied for the $x$- and $y$-components of the displacement field due to the use of KUBCs Eq. (48), we do not constraint it along the $z$-component of the displacement field to reduce the number of constraints in the system. Indeed, not enforcing this condition corresponds to the impossibility to constrain high-order deformation modes which are not down-scaled from the Kirchhoff-Love plate kinematics as it will be discussed in Section 3.3, and has thus no effect on the homogenization result.



*Prepared using* nmeauth.cls
DOI: 10.1002/nme

### *3.3. Computational homogenization and extraction of the resultant material tensor* $\boldsymbol{U}$

In the context of the meso-scale BVP resolution, the tangent matrix of the second-order multi-scale process can be extracted by condensing the micro-scale stiffness matrix using the boundary condition constraints, as detailed in [55, 56]. In case of linear elasticity, this tangent matrix corresponds to the homogenized material operators, yielding

$$\boldsymbol{n}_M = \mathbb{C}_1 : \boldsymbol{\upsilon}_M + \mathbb{C}_2 \vdots \boldsymbol{\eta}_M \,, \tag{52}$$

$$\tilde{\boldsymbol{m}}_M = \mathbb{C}_3 : \boldsymbol{\upsilon}_M + \mathbb{C}_4 \vdots \boldsymbol{\eta}_M \,, \tag{53}$$

where $\mathbb{C}_1$, $\mathbb{C}_2$, $\mathbb{C}_3$, and $\mathbb{C}_4$ are respectively a fourth order tensor, two fifth order tensors, and one sixth order tensor.

However, in the context of plates at the macro-scale, the relevant material tensors are the resultant material tensors $\mathbb{C}_1^*$, $\mathbb{C}_2^*$, $\mathbb{C}_3^*$, and $\mathbb{C}_4^*$ defined in Eqs. (16-17), or in the matrix form, the resultant tensor $\boldsymbol{U}$ defined in Eq. (18). We thus need to extract the resultant tensors from the homogenized tensors $\mathbb{C}_1$, $\mathbb{C}_2$, $\mathbb{C}_3$, and $\mathbb{C}_4$. To this end, the kinematic constraints and the homogenized properties resulting from the meso-scale BVP resolution, see Fig. 1(b), can be written in terms of their components.

The homogenized symmetric first-order stress tensor has 6 independent components and is expressed as:

$$\boldsymbol{n}_M = \tilde{\boldsymbol{n}}^{*\alpha\beta} \boldsymbol{E}_\alpha \otimes \boldsymbol{E}_\beta + \tilde{\boldsymbol{q}}^{*\alpha} (\boldsymbol{E}_\alpha \otimes \boldsymbol{E}_z + \boldsymbol{E}_z \otimes \boldsymbol{E}_\alpha) + \tilde{\boldsymbol{n}}^{zz} \boldsymbol{E}_z \otimes \boldsymbol{E}_z \,, \tag{54}$$

where $\tilde{\boldsymbol{n}}_{zz} = 0$ is naturally enforced during the meso-scale BVP resolution as the top and bottom surfaces are stress-free surfaces, see Section 3.2. The homogenized second-order stress tensor has 18 independent components. Considering the symmetric $2 \times 2$ matrix $\tilde{\boldsymbol{m}}^{*\alpha\beta}$, the component $\tilde{\boldsymbol{m}}^{\text{skew}\,xy} = -\tilde{\boldsymbol{m}}^{\text{skew}\,yx}$ related to the lack of major symmetry in $\tilde{\boldsymbol{m}}_M$, the $2 \times 2$ symmetric matrix $\boldsymbol{p}^{1\alpha\beta}$, the 2-component vectors $\boldsymbol{p}^{2\alpha}$ and $\boldsymbol{p}^{3\alpha}$, and the component $\tilde{\boldsymbol{m}}^{zz}$, the homogenized second-order stress



*Prepared using* nmeauth.cls
DOI: 10.1002/nme

tensor reads

$$\begin{aligned}\tilde{\boldsymbol{m}}_M &= \left(\tilde{\boldsymbol{m}}^{*\alpha\beta}+\tilde{\boldsymbol{m}}^{\mathrm{skew}\,\alpha\beta}\right)\left(\boldsymbol{E}_\alpha\otimes\boldsymbol{E}_\beta\otimes\boldsymbol{E}_z+\boldsymbol{E}_\alpha\otimes\boldsymbol{E}_z\otimes\boldsymbol{E}_\beta\right)+\boldsymbol{p}^{1\,\alpha\beta}\left(\boldsymbol{E}_z\otimes\boldsymbol{E}_\alpha\otimes\boldsymbol{E}_\beta\right)\\ &+ \boldsymbol{p}^{2\,\alpha}\left(\boldsymbol{E}_z\otimes\boldsymbol{E}_z\otimes\boldsymbol{E}_\alpha+\boldsymbol{E}_z\otimes\boldsymbol{E}_\alpha\otimes\boldsymbol{E}_z\right)+\boldsymbol{p}^{3\,\alpha}\left(\boldsymbol{E}_\alpha\otimes\boldsymbol{E}_z\otimes\boldsymbol{E}_z\right)+\\ &\quad \tilde{\boldsymbol{m}}^{zz}\boldsymbol{E}_z\otimes\boldsymbol{E}_z\otimes\boldsymbol{E}_z+\hat{\tilde{\boldsymbol{m}}}_M,\end{aligned}\tag{55}$$

where $\hat{\tilde{\boldsymbol{m}}}_M$ represents the contribution of the 6 remaining independent components along $\boldsymbol{E}_\alpha\otimes\boldsymbol{E}_\beta\otimes\boldsymbol{E}_\gamma$. Owing to the plane-stress state, $\tilde{\boldsymbol{m}}^{zz}=0$ is naturally enforced during the meso-scale BVP resolution. Similarly $\boldsymbol{p}^{1\,xy}=\boldsymbol{p}^{1\,yx}=0$, and $\boldsymbol{p}^{2\,\alpha}=0$ are also verified because of the plane-stress state.

The symmetric first-order kinematic constraint $\boldsymbol{\varepsilon}_M$ possesses 6 independent components and can be written as

$$\boldsymbol{\varepsilon}_M=\boldsymbol{\varepsilon}^*_{\alpha\beta}\boldsymbol{E}_\alpha\otimes\boldsymbol{E}_\beta+\boldsymbol{\gamma}^*_\alpha\left(\boldsymbol{E}_\alpha\otimes\boldsymbol{E}_z+\boldsymbol{E}_z\otimes\boldsymbol{E}_\alpha\right)+\boldsymbol{\varepsilon}^*_{zz}\boldsymbol{E}_z\otimes\boldsymbol{E}_z,\tag{56}$$

where $\boldsymbol{\varepsilon}^*_{\alpha\beta}$ is a $2\times2$ symmetric matrix defining the membrane deformation. In this expression, the out-of-plane strain $\boldsymbol{\varepsilon}^*_{zz}$ is an unknown not necessarily defined in the macro-scale plate problem, and is not down-scaled during the multi-scale process as its value results from the plane-stress state. The second-order kinematic constraint is written as:

$$\begin{aligned}\boldsymbol{\eta}_M &= \left(\boldsymbol{\kappa}^*_{\alpha\beta}+\boldsymbol{\kappa}^{\mathrm{skew}}_{\alpha\beta}\right)\left(\boldsymbol{E}_\alpha\otimes\boldsymbol{E}_\beta\otimes\boldsymbol{E}_z+\boldsymbol{E}_\alpha\otimes\boldsymbol{E}_z\otimes\boldsymbol{E}_\beta\right)+\boldsymbol{b}^1_{\alpha\beta}\left(\boldsymbol{E}_z\otimes\boldsymbol{E}_\alpha\otimes\boldsymbol{E}_\beta\right)\\ &+ \boldsymbol{b}^2_\alpha\left(\boldsymbol{E}_z\otimes\boldsymbol{E}_z\otimes\boldsymbol{E}_\alpha+\boldsymbol{E}_z\otimes\boldsymbol{E}_\alpha\otimes\boldsymbol{E}_z\right)+\boldsymbol{b}^3_\alpha\left(\boldsymbol{E}_\alpha\otimes\boldsymbol{E}_z\otimes\boldsymbol{E}_z\right)+\\ &\quad \boldsymbol{b}_{zz}\boldsymbol{E}_z\otimes\boldsymbol{E}_z\otimes\boldsymbol{E}_z+\hat{\boldsymbol{\eta}}_M,\end{aligned}\tag{57}$$

where $\boldsymbol{\kappa}^*_{\alpha\beta}$ is a $2\times2$ symmetric matrix containing the bending curvatures so that $\boldsymbol{\kappa}^*_{\alpha\beta}=\frac{\boldsymbol{\eta}_{M\alpha\beta z}+\boldsymbol{\eta}_{M\beta\alpha z}}{2}$, $\boldsymbol{\kappa}^{\mathrm{skew}}_{xy}=-\boldsymbol{\kappa}^{\mathrm{skew}}_{yx}$ is the skewness, $\boldsymbol{b}^1_{\alpha\beta}$ is a $2\times2$ symmetric matrix, $\boldsymbol{b}^2_\alpha$ and $\boldsymbol{b}^3_\alpha$ are 2-component vectors, $\boldsymbol{b}_{zz}$ is a scalar, and where $\hat{\boldsymbol{\eta}}_M$ represents the contribution of the 6 remaining independent components along $\boldsymbol{E}_\alpha\otimes\boldsymbol{E}_\beta\otimes\boldsymbol{E}_\gamma$. In the frame of plate elements, the higher-order strain components $\boldsymbol{b}^1_{xy}=\boldsymbol{b}^1_{yx}$, $\boldsymbol{b}^2_\alpha$, and $\boldsymbol{b}_{zz}$ are four components that are not down-scaled from the macro-scale as their values result from the plane-stress state.



*Prepared using* nmeauth.cls
DOI: 10.1002/nme

Five equations linking the homogenized stresses ($\tilde{\boldsymbol{n}}_{zz}=0$, $\boldsymbol{p}^{1\,xy}=\boldsymbol{p}^{1\,yx}=0$, $\boldsymbol{p}^{2\,\alpha}=0$, and $\tilde{\boldsymbol{m}}^{zz}=0$[‖]) to the kinematic constraints can thus be directly removed from the system (52-53) as five kinematic constraints ($\boldsymbol{\varepsilon}^{*}_{zz}$, $\boldsymbol{b}^{1}_{xy}=\boldsymbol{b}^{1}_{yx}$, $\boldsymbol{b}^{2}_{\alpha}$, and $\boldsymbol{b}_{zz}$) result from the boundary conditions constraining the plane-stress state.

Moreover, as the plate elements at the macro-scale follow the Kirchhoff-Love assumption and as this hypothesis is not applied on the RSVE itself during the computational homogenization, the contribution of some stresses is explicitly enforced to zero to recover the behavior associated to this assumption. Therefore the remaining system of 19 equations linking 19 homogenized stress components to 19 kinematic constraints components can be reduced. The out-of-plane shear $\tilde{\boldsymbol{q}}^{*\,\alpha}$ is enforced to be zero. Similarly, the influence of the out-of-plane shear on the higher-order stress, obtained through $\boldsymbol{p}^{1\,\alpha\alpha}$ (no sum on $\alpha$ meant), $\boldsymbol{p}^{3\,\alpha}$, and through the skew-symmetric matrix $\tilde{\boldsymbol{m}}^{\mathrm{skew}\,xy}$, are enforced to zero. As the elements of $\hat{\tilde{\boldsymbol{m}}}_{M}$ cannot be up-scaled to the plate problem, they are also enforced to zero. We thus gather those stress contributions to be enforced to zero in the 13-component vector (no sum on $\alpha$ meant)

$$\boldsymbol{\psi}_0=\left[\boldsymbol{q}^{*\,\alpha},\tilde{\boldsymbol{m}}^{\mathrm{skew}\,xy},\boldsymbol{p}^{1\,\alpha\alpha},\boldsymbol{p}^{3\,\alpha},\hat{\tilde{\boldsymbol{m}}}_{M}{}^{\alpha\beta\gamma}\right]. \tag{58}$$

The corresponding strain components, which are not down-scaled from the macro-scale plate model, are gathered in the 13-component vector (no sum on $\alpha$ meant)

$$\boldsymbol{\chi}_u=\left[\boldsymbol{\gamma}^{*}_{\alpha},\boldsymbol{\kappa}^{\mathrm{skew}}_{xy},\boldsymbol{b}^{1}_{\alpha\alpha},\boldsymbol{b}^{3}_{\alpha},\hat{\boldsymbol{\eta}}_{M\,\alpha\beta\gamma}\right]. \tag{59}$$

Once the plane-stress state and the Kirchhoff-Love assumption being considered, the remaining stresses are the resultant (symmetric) membrane stress $\tilde{\boldsymbol{n}}^{*}$ and the resultant (symmetric) bending stress $\tilde{\boldsymbol{m}}^{*}$. These symmetric matrices can be written in terms of the 6-component vector

$$\boldsymbol{\psi}^{\star}_{\sigma}=\left[\tilde{\boldsymbol{n}}^{*\,\alpha\beta},\tilde{\boldsymbol{m}}^{*\,\alpha\beta}\right]. \tag{60}$$

[‖]For ease of implementation, the RSVE centroïd is defined as the center of the parallelepiped defined using the average plane of the rough-surface and is thus not exactly the RSVE centroïd, so these terms are several orders of magnitude lower than the other ones but not strictly zero as Eq. (35) is not exactly satisfied.



*Prepared using* nmeauth.cls
DOI: 10.1002/nme

Similarly, the relevant 6 independent strains are the elements of the (symmetric) membrane strains $\boldsymbol{\varepsilon}^*$ and the (symmetric) curvatures $\boldsymbol{\kappa}^*$, which can be written in terms of the 6-component vector

$$\boldsymbol{\chi}_{\varepsilon}^{\star} = \left[\boldsymbol{\varepsilon}_{\alpha\beta}^{*}, \boldsymbol{\kappa}_{\alpha\beta}^{*}\right]. \tag{61}$$

Therefore, the linear system (52-53) is reorganized into the system

$$\begin{pmatrix} \boldsymbol{\psi}_{\sigma}^{\star} \\ \boldsymbol{\psi}_{0} \end{pmatrix} = \begin{pmatrix} \mathbf{C}_{\varepsilon\varepsilon} & \mathbf{C}_{\varepsilon u} \\ \mathbf{C}_{u\varepsilon} & \mathbf{C}_{uu} \end{pmatrix} \begin{pmatrix} \boldsymbol{\chi}_{\varepsilon}^{\star} \\ \boldsymbol{\chi}_{u} \end{pmatrix}, \tag{62}$$

where the $\mathbf{C}_{ik}$ elements are matrices obtained from the different tangents $\mathbb{C}_i$. As $\boldsymbol{\psi}_0 = \mathbf{0}$ is enforced, this system reduces to

$$\boldsymbol{\psi}_{\sigma}^{\star} = \left(\mathbf{C}_{\varepsilon\varepsilon} + \mathbf{C}_{\varepsilon u}\mathbf{C}_{uu}^{-1}\mathbf{C}_{u\varepsilon}\right)\boldsymbol{\chi}_{\varepsilon}^{\star}. \tag{63}$$

Finally, the resultant material tensor $\boldsymbol{U}$, the $6\times 6$ matrix already introduced in Section 2.1 and defined by Eq. (18), is retrieved as the linear operator between $\boldsymbol{\psi}_{\sigma}^{\star}$ and $\boldsymbol{\chi}_{\varepsilon}^{\star}$:

$$\boldsymbol{U}(\boldsymbol{x},\boldsymbol{\theta}) = \left(\mathbf{C}_{\varepsilon\varepsilon} + \mathbf{C}_{\varepsilon u}\mathbf{C}_{uu}^{-1}\mathbf{C}_{u\varepsilon}\right). \tag{64}$$

### *3.4. Verification*

In order to verify the homogenization process we consider a homogeneous parallelepiped volume element of size $0.5\times 0.4\times 0.1\ \mu\text{m}^3$ with uniform material properties of Young's modulus $E = 160$ GPa and Poisson coefficient $\nu = 0.28$. The Kirchhoff-Love plate theory predicts the following material tensors

$$\mathbb{C}_1^{*\alpha\beta\gamma\delta} = \frac{Eh}{1-\nu^2}\left[\nu\delta^{\alpha\beta}\delta^{\gamma\delta} + \frac{1-\nu}{2}\left(\delta^{\alpha\gamma}\delta^{\beta\delta} + \delta^{\alpha\delta}\delta^{\beta\gamma}\right)\right], \text{ and} \tag{65}$$

$$\mathbb{C}_4^{*\alpha\beta\gamma\delta} = \frac{Eh^3}{12(1-\nu^2)}\left[\nu\delta^{\alpha\beta}\delta^{\gamma\delta} + \frac{1-\nu}{2}\left(\delta^{\alpha\gamma}\delta^{\beta\delta} + \delta^{\alpha\delta}\delta^{\beta\gamma}\right)\right]. \tag{66}$$

The results obtained with the homogenization process (64) are compared to the analytical predictions (65-66) in Table I. An excellent agreement (error below 0.005%) is observed between the two methods.



*Prepared using* nmeauth.cls
DOI: 10.1002/nme

Table I. Verification of the homogenization process on a homogeneous meso-scale volume element

| | Analytical, Eqs. (65-66) | Homogenization, Eq. (64) |
|---|---|---|
| $\mathbb{C}_1^{*(1111)} = \boldsymbol{U}^{(11)}$ [GPa $\cdot\mu$m] | 17.361111 | 17.361111 |
| $\mathbb{C}_1^{*(1122)} = \boldsymbol{U}^{(12)}$ [GPa $\cdot\mu$m] | 4.861111 | 4.861111 |
| $\mathbb{C}_1^{*(1212)} = \boldsymbol{U}^{(33)}$ [GPa $\cdot\mu$m] | 6.25 | 6.25 |
| $\mathbb{C}_4^{*(1111)} = \boldsymbol{U}^{(44)}$ [GPa $\cdot\mu$m$^3$] | 0.0144676 | 0.0144683 |
| $\mathbb{C}_4^{*(1122)} = \boldsymbol{U}^{(45)}$ [GPa $\cdot\mu$m$^3$] | 0.00405092 | 0.00404984 |
| $\mathbb{C}_4^{*(1212)} = \boldsymbol{U}^{(66)}$ [GPa $\cdot\mu$m$^3$] | 0.00520833 | 0.00520833 |

## 4. STOCHASTIC MODEL FOR THE MESO-SCALE MATERIAL AND GEOMETRICAL PROPERTIES

As discussed in Section 2.1, two correlated random fields are required as input for the macro-scale plate SFEM: the resultant material properties matrix $\boldsymbol{U}(\boldsymbol{x},\boldsymbol{\theta}) : \mathcal{A}\times\boldsymbol{\Omega} \rightarrow \boldsymbol{M}_N^{+s}(\mathbb{R})$ and the mass per membrane surface unit area $\bar{\rho}(\boldsymbol{x},\boldsymbol{\theta}) : \mathcal{A}\times\boldsymbol{\Omega} \rightarrow R^+$. Although building a stochastic model to generate these correlated fields is not compulsory, this simplifies the macro-scale computation. Indeed, without a stochastic model, a (R)SVE must be generated and solved with the computational homogenization process at each integration point of the macro-scale SFEM, which is computationally expensive. Solving the macro-scale SFEM having recourse to a stochastic model is a two-step process. The first one involves the computation of enough (R)SVEs to capture its stochastic behavior, including the spatial correlation, and the construction of a stochastic model using those realizations. The second step is the macro-scale SFEM resolutions: for each realization of the macro-scale problem, the stochastic model is called to generate the meso-scale properties of interest (the random fields) at each integration point, and the macro-scale finite element model can then be solved directly. This section deals with the definition of an appropriate stochastic model.



*Prepared using* nmeauth.cls DOI: 10.1002/nme

### *4.1. The lower bound definition*

As emphasized in [57], a relevant stochastic model of a positive-definite matrix is obtained when the existence of the expectation of the norm of the inverse of the matrix of interest can be proven:

$$\mathbb{E}\left[\left(\sup_{\boldsymbol{x}\in\mathcal{A}}\left\|\left(\boldsymbol{U}(\boldsymbol{x},\boldsymbol{\theta})\right)^{-1}\right\|\right)^2\right] = c^2 < +\infty, \tag{67}$$

where "sup" is the supremum and $c$ is a finite positive constant. As shown in [50] or [1, Appendix A], the introduction of a lower bound guarantees the respect of this property. Therefore, to ensure an appropriate generation of $\boldsymbol{U}$, a lower bound is defined and enforced.

In this paper, the lower bound is based on the available samples of $\boldsymbol{U}$, as was already done in [58] for the generation of elasticity tensors, and is thus defined by

$$\boldsymbol{U}_L = \lambda_L \boldsymbol{I}_6\,, \tag{68}$$

where $\lambda_L$ is $\lambda_L = \varepsilon\lambda_{\min}$, with $\varepsilon$ a tolerance parameter arbitrarily fixed to 0.95 and $\lambda_{\min}$ the smallest eigenvalue of all the computed samples of $\boldsymbol{U}$, and where $\boldsymbol{I}_N$ is the identity matrix of size $N \times N$.

Similarly, the mass matrix should be strictly positive as it has to be inverted in a eigen frequency analysis. Therefore we define

$$\bar{\rho}_L = \varepsilon\bar{\rho}_{\min}\,, \tag{69}$$

where $\bar{\rho}_{\min}$ is the smallest mass per unit area of all the computed samples.

### *4.2. The Gaussian random field generator*

A similar approach as the one developed in [1] is considered in this paper in order to generate bounded symmetric material tensors $\boldsymbol{U}$. However, in the current context, this is not the only property that must be generated: the mass density per membrane unit area $\bar{\rho}$, which should remain strictly positive, is also required and is correlated to $\boldsymbol{U}$.

First, a semi-positive definite symmetric increment $\Delta\boldsymbol{U}$ is defined such that

$$\boldsymbol{U} = \boldsymbol{U}_L + \Delta\boldsymbol{U}\,, \tag{70}$$



*Prepared using* nmeauth.cls
DOI: 10.1002/nme

is always a symmetric positive definite matrix, bounded by $\boldsymbol{U}_L$. To generate such a semi-positive-definite matrix, one can use the Cholesky decomposition as described in [57], which reads

$$\Delta \boldsymbol{U} = \boldsymbol{L}\boldsymbol{L}^T . \tag{71}$$

In this equation, the matrix $\boldsymbol{L}$ is a lower triangular matrix and the superscript "$T$" refers to the transposed matrix. The matrix $\boldsymbol{L}$ is made of 21 independent entries, which form a random vector field.

The lower bound of the mass densities per membrane unit area $\bar{\rho}$ is enforced by defining

$$\bar{\rho} = \bar{\rho}_L + \Delta\bar{\rho} , \tag{72}$$

where $\Delta\bar{\rho}$ has to be enforced to be positive.

In this work a vector field $\boldsymbol{a}$ of 22 elements is considered: the 21 elements of $\boldsymbol{L}$ as well as the logarithmic mapping $\boldsymbol{a}^{(22)} = \log(\Delta\bar{\rho})$, which enforces the positive nature of $\Delta\bar{\rho}$. Let $\bar{\boldsymbol{a}} = \mathbb{E}[\boldsymbol{a}]$, $\sigma_{\boldsymbol{a}} = \sqrt{\mathbb{E}\left[(\boldsymbol{a} - \mathbb{E}[\boldsymbol{a}])^2\right]}$ and $\boldsymbol{a}'$ be respectively the mean or expectation, the standard deviation, and the normalized fluctuation of the elements of $\boldsymbol{a}$ so that the random vector field reads

$$\boldsymbol{a}^{(r)} = \bar{\boldsymbol{a}}^{(r)} + \boldsymbol{a}'^{(r)}\sigma_{\boldsymbol{a}^{(r)}} , \tag{73}$$

where $\boldsymbol{a}^{(r)}$ denotes the $r^{th}$ entry in $\boldsymbol{a}$. The zero-mean fluctuations $\boldsymbol{a}'^{(r)}$ are normalized with their standard deviation in order to be able to generate values for the different entries of $\boldsymbol{a}$ which are different by several orders of magnitude.

This random field $\boldsymbol{a}'(\boldsymbol{x}, \boldsymbol{\theta})$ can be generated using the spectral representation method [46] by following the different steps detailed in [1, Appendix C]:

(i) The symmetric material tensors $\boldsymbol{U}$ and mass densities per membrane unit area $\bar{\rho}$ of SVE realizations are obtained using the framework described in Section 3.3. The different SVEs are extracted from several larger micro-structure models and, in each of such a micro-structure model, the centers of the different SVEs are separated by a vector $\boldsymbol{\tau}$, following a moving-window technique [43], as illustrated in 2D in Fig. 3 and as it will be illustrated for the particular case of RSVEs in Section 5.2.3.



*Prepared using* nmeauth.cls DOI: 10.1002/nme

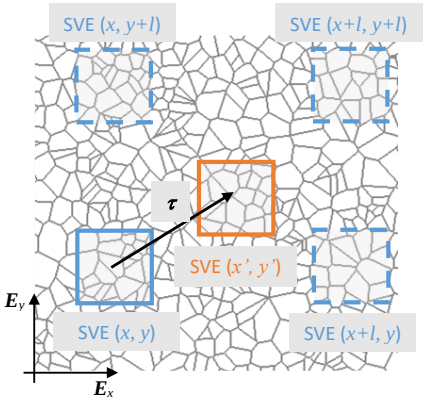


Figure 3. 2D illustration of the moving-window technique on a distance $l$ to extract SVEs whose centers are separated by the vector $\boldsymbol{\tau}$

(ii) The random vector field entries $\boldsymbol{a}'^{(r)}$, $r = 1, ..., 22$, are computed for each SVE realization using successively Eqs. (70-73).

(iii) The discrete spatial auto- and cross-correlations are computed using their definition, with for the couple of entries $r, s = 1, ..., 22$

$$\boldsymbol{R}_{\boldsymbol{a}'}^{(rs)}(\boldsymbol{\tau}) = \mathbb{E}\left[\boldsymbol{a}'^{(r)}(\boldsymbol{0})\, \boldsymbol{a}'^{(s)}(\boldsymbol{\tau})\right]. \tag{74}$$

This spatial correlation $\boldsymbol{R}_{\boldsymbol{a}'}(\boldsymbol{\tau})$ is only computed for a limited spatial distance. Larger fields can be generated by considering a zero-padding as soon as the spatial correlation reaches zero.

(iv) From the evaluation of $\boldsymbol{R}_{\boldsymbol{a}'}^{(rs)}(\boldsymbol{\tau})$, its corresponding spectral density $\boldsymbol{S}_{\boldsymbol{a}'}^{(rs)}(\boldsymbol{k})$, where $\boldsymbol{k}$ is defined in the frequency domain, is computed using the Fourier transforms.

(v) From the spectral density $\boldsymbol{S}_{\boldsymbol{a}'}(\boldsymbol{k})$, a Gaussian random field can be generated according to:

$$\boldsymbol{a}'^{(r)}(\boldsymbol{x}, \boldsymbol{\theta}) = \sqrt{2\Delta}\,\mathrm{Re}\left[\sum_{s=1}^{22}\sum_{\boldsymbol{m}=\boldsymbol{0}}^{\boldsymbol{N}-\boldsymbol{I}} \boldsymbol{H}_{\boldsymbol{a}'}^{(rs)}(\boldsymbol{k}_{\boldsymbol{m}})\, \boldsymbol{\eta}_{s,\boldsymbol{k}_{\boldsymbol{m}}} e^{2\pi i(\boldsymbol{x}\cdot\boldsymbol{k}_{\boldsymbol{m}} + \boldsymbol{\theta}_{s,\boldsymbol{k}_{\boldsymbol{m}}})}\right] \tag{75}$$

where $\boldsymbol{S}_{\boldsymbol{a}'} = \boldsymbol{H}_{\boldsymbol{a}'}\boldsymbol{H}_{\boldsymbol{a}'}^{\star}$, with $\boldsymbol{H}_{\boldsymbol{a}'}^{\star}$ the conjugate transpose of $\boldsymbol{H}_{\boldsymbol{a}'}$, $\Delta$ is a parameter depending on the increment of $\boldsymbol{k}$ in the frequency domain, $\boldsymbol{m}$ is a multi-dimensional index covering the frequency space, $\boldsymbol{\eta}_{s,\boldsymbol{k}_{\boldsymbol{m}}} = \sqrt{-\log \boldsymbol{\psi}_{s,\boldsymbol{k}_{\boldsymbol{m}}}}$, and $\boldsymbol{\theta}_{s,\boldsymbol{k}_{\boldsymbol{m}}}$, $\boldsymbol{\psi}_{s,\boldsymbol{k}_{\boldsymbol{m}}}$ are uniformly distributed independent random variables defined for each variable $s$ and each frequency $\boldsymbol{k}_{\boldsymbol{m}}$. Details can be found in [1].



*Prepared using* nmeauth.cls
DOI: 10.1002/nme

(vi) Although Eq. (75) can be directly used to generate a random field evaluated at any position $\boldsymbol{x}$ of interest, for large fields this can involve a computational burden, which can be avoided with the help of the Fast Fourier Transforms. Equation (75) is first solved with FFTs on a predefined spatial grid. The field values $\boldsymbol{a}'^{(r)}(\boldsymbol{x}, \boldsymbol{\theta})$ at any spatial position $\boldsymbol{x}$ are then retrieved by recourse to an interpolation procedure.

### *4.3. Non-Gaussian extension*

Equation (75) produces, once converged, zero-mean normalized Gaussian $\boldsymbol{a}'^{(r)}$ values whose correlation functions follow Eq. (74). When the targeted distribution of $\boldsymbol{a}'^{(r)}$ are far from being Gaussian, it may be relevant to consider a non-Gaussian mapping to improve the generated marginal probability distribution while loosing some accuracy in the spectral density and thus in the spatial correlation and cross-correlation.

The Non-Gaussian generation process that is followed in this work is described in [47, 48, 49]. It involves the following steps:

(i) First, from the targeted spectral density $\boldsymbol{S}^{\text{Target}}$, Gaussian samples are obtained using the process described in Section 4.2. These Gaussian samples are then mapped to the sought non-Gaussian distribution thanks to their cumulative distribution function.

(ii) From these samples, the generated spectral density $\boldsymbol{S}^{\text{Generated}}$ is computed. If the latter is different from the targeted spectral density, an iterative procedure is used to have a closer match between the two spectral densities. A new density, $\boldsymbol{S}^{\text{iteration}}$, is updated and used at each iteration to produce Gaussian variables that are mapped once again to the non-Gaussian distribution of interest. The corresponding spectral density $\boldsymbol{S}^{\text{Generated}}$ can then be updated.

(iii) This process will be repeated until $\boldsymbol{S}^{\text{Target}} \approx \boldsymbol{S}^{\text{Generated}}$ at a given tolerance.

Details on this iterative process, with convergence improvements as compared to the literature, can be found in [37].

The properties of interest are then obtained by following the reverse path of Eqs. (70-73). The bounded symmetric material tensors $\boldsymbol{U}$ are retrieved at each position $\boldsymbol{x}$ from the generated random



*Prepared using* nmeauth.cls
DOI: 10.1002/nme

field according to

$$\boldsymbol{U}(\boldsymbol{x},\boldsymbol{\theta}) = \boldsymbol{U}_L + \boldsymbol{L}(\bar{\boldsymbol{a}} + \boldsymbol{a}'(\boldsymbol{x},\boldsymbol{\theta})\,\sigma_{\boldsymbol{a}})\,\boldsymbol{L}(\bar{\boldsymbol{a}} + \boldsymbol{a}'(\boldsymbol{x},\boldsymbol{\theta})\,\sigma_{\boldsymbol{a}})^T\ , \tag{76}$$

and the mass density per membrane unit area $\bar{\rho}$, is retrieved at each position $\boldsymbol{x}$ according to

$$\bar{\rho}(\boldsymbol{x},\boldsymbol{\theta}) = \bar{\rho}_L + e^{\left(\bar{\boldsymbol{a}}^{(22)} + \boldsymbol{a}'^{(22)}(\boldsymbol{x},\boldsymbol{\theta})\sigma_{\boldsymbol{a}^{(22)}}\right)}\ . \tag{77}$$

## 5. APPLICATION TO MEMS POLY-SILICON THIN STRUCTURES

The procedure described in the previous sections is now applied on MEMS thin structures. First of all, the manufacture process of the poly-silicon thin structures and the performed experimental measurements are briefly explained in Section 5.1. The (R)SVEs are generated based on these experimental measurements in Section 5.2. Then, the stochastic behavior of the meso-scale (R)SVEs homogenized properties is investigated in Section 5.3. In Section 5.4, a stochastic model is constructed and the generated random fields are compared to the computed micro-scale stochastic behavior. The probabilistic behavior of the MEMS thin structures is then predicted in Section 5.5 by using the plate SFEM, with as input the generated random fields. Finally the computation costs related to the different steps are detailed in Section 5.6.

### *5.1. Poly-silicon processing*

*5.1.1. Low Pressure Vapor Chemical Deposition process* The thin structures are made of poly-silicon, one of the most common material present in MEMS using Low Pressure Chemical Vapor Deposition (LPCVD) technique. From the $< 100 >$ orientation silicon wafer of p-type, a silicon dioxide layer was grew by thermal technique at 1000 °C. Columnar polycrystalline silicon was thus deposited on this silicon dioxide layer. The micro structure, such as grain orientation and size, varies with the deposition temperature and time. Samples obtained for the successive temperatures of 580°C, 610°C, 630°C, and 650°C, were manufactured at pressure of 0.267 mbar and with a Silane flow of respectively 15, 15, 20, and 25 sccm. The thickness of the samples is about 2 $\mu$m,



*Prepared using* nmeauth.cls DOI: 10.1002/nme

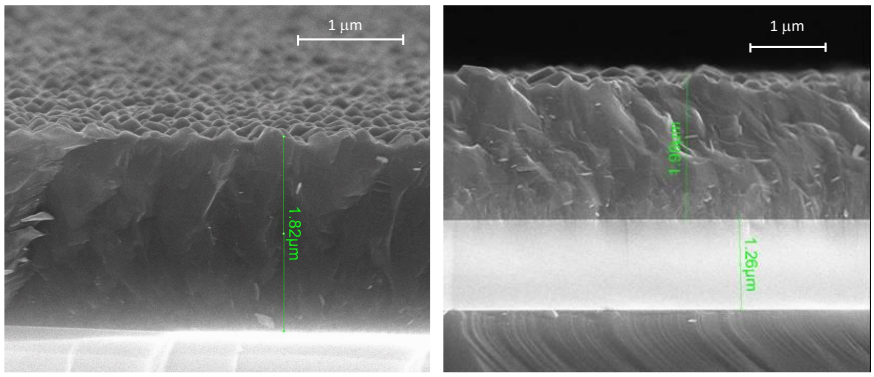


(a) 580°C (b) 610°C

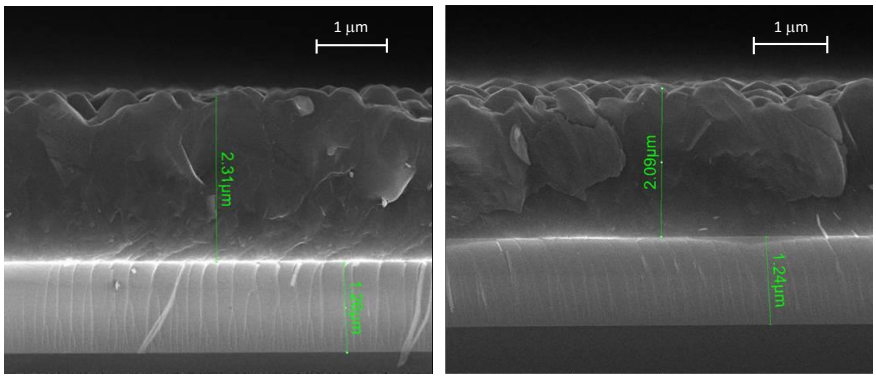


(c) 630°C (d) 650°C

Figure 4. Cross-section SEM images for different temperatures of the fabrication process

respectively 1.82 $\mu$m, 1.98 $\mu$m, 2.31 $\mu$m, and 2.09 $\mu$m for the four temperatures, as illustrated in the cross-section views in Fig. 4.

*5.1.2. Measurements* The measurements are the starting point for the definition of the (R)SVEs. Three types of measurements are available for the poly-silicon layers obtained at the different deposition temperatures.

(i) Scanning Electron Microscope (SEM) images for the grain size analyses;

(ii) X-Ray Diffraction (XRD) measurements for the grain orientation distribution analyses;



*Prepared using* nmeauth.cls DOI: 10.1002/nme

(iii) Atomic-force microscopy (AFM) measurements for the top surface roughness (the bottom surface roughness being of several orders lower).

First, top views of the films obtained from SEM images are shown for the different deposition temperatures in Fig. 5, *i.e.* for temperatures of 580°C, 610°C, 630°C, and 650°C. Processing the images allows obtaining the grain size distributions for the different temperature cases. The average grain diameters, for the different temperatures of the fabrication process, are reported in Table II, where it can be seen that the grain size strongly depends on the temperature of the fabrication process.

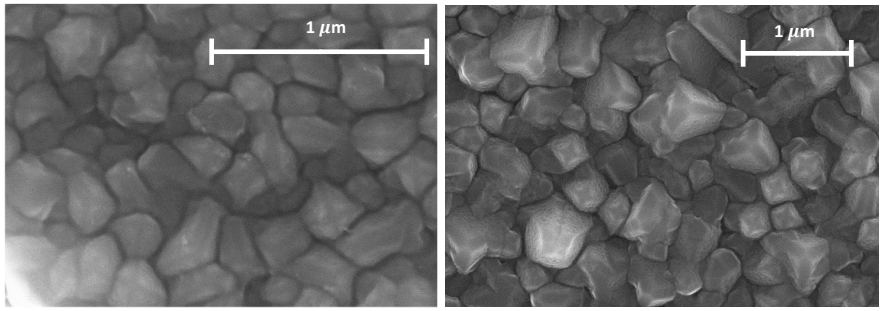


(a) 580°C (b) 610°C

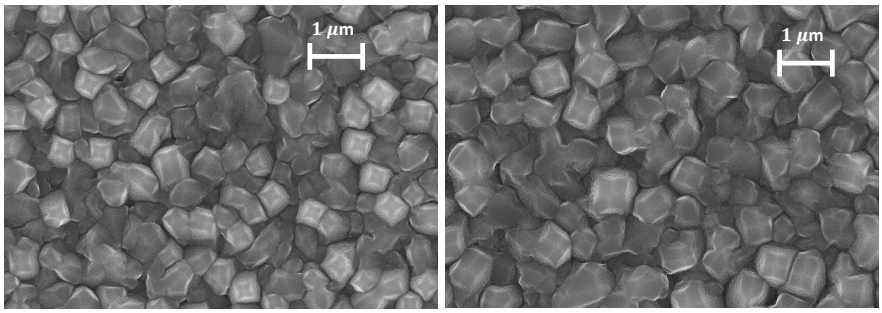


(c) 630°C (d) 650°C

Figure 5. SEM images (top view) for the different temperatures of the fabrication process

The XRD results are reported in Fig. 6 for the different deposition temperatures. From the XRD measurements, the crystallinity is always higher than 97.48%. Therefore no amorphous phase is



*Prepared using* nmeauth.cls
DOI: 10.1002/nme

Table II. Average grain diameter for the different temperatures of the fabrication process

| **Deposition temperature** [°C] | 580 | 610 | 630 | 650 |
|---|---|---|---|---|
| **Average grain diameter** [$\mu$m] | 0.21 | 0.447 | 0.7195 | 0.83 |

considered in this work. The XRD-measurements also provide information about the relative weight fraction for the different orientations.

With high quality data, we can determine how much of each phase is present. The ratio of peak intensity $I$ varies linearly as a function of weight fractions for any two phases in a mixture. Here the two phases refer to poly-silicon grains with two different orientations ($\alpha$ and $\beta$) towards the surface of the measured sample. Assuming that their weight fractions are $X_\alpha$ and $X_\beta$, respectively, we have

$$\frac{I_\alpha}{I_\beta} = \frac{I^0_\alpha (I/I_{\text{cor}})_\beta X_\alpha}{I^0_\beta (I/I_{\text{cor}})_\alpha X_\beta}, \tag{78}$$

where

$$\frac{I}{I_{\text{cor}}} = \frac{\text{Intensity of sample' s 100\% peak}}{\text{Intensity of Corundum' s 100\% peak}}, \tag{79}$$

and where $I^0_*$ is the reference relative intensity. For silicon we have

$$\frac{I}{I_{\text{cor}}} = 4.7 \quad \text{and} \quad I(111) = 100\%, \tag{80}$$

and the reference relative intensities ($I^0_* = I_*/I(111)$ according to powder XRD measurements) are reported in Table III. Applying these formula on the XRD measurements reported in Fig. 6 yields

Table III. Reference relative intensity with respect to the direction $< 111 >$ for silicon [59]

| **Orientation** | $< 111 >$ | $< 220 >$ | $< 311 >$ | $< 400 >$ | $< 331 >$ | $< 422 >$ |
|---|---|---|---|---|---|---|
| $\mathbf{I^0_*}$ [%] | 100 | 55 | 30 | 6 | 11 | 12 |

the results in terms of weight fractions, with a crystallinity of 100% considered, as reported in Table IV.

The influence of the XRD-based orientation on the Young's modulus distribution for a single crystal is investigated in Fig. 7, in which two different cases are considered: in Fig. 7(a), the



*Prepared using* nmeauth.cls DOI: 10.1002/nme

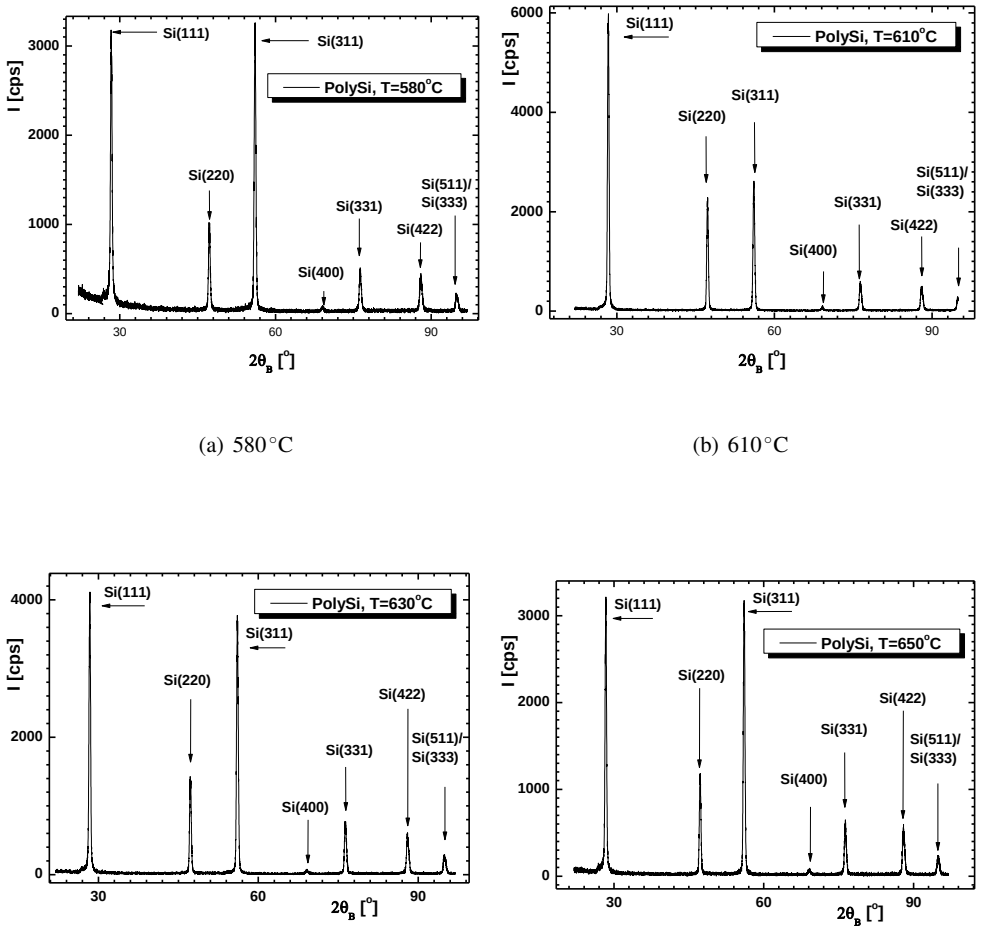


(a) 580 °C (b) 610 °C

(c) 630 °C (d) 650 °C

Figure 6. XRD measurements for different temperatures of the fabrication process. The intensity of each peak, associated to one orientation, is given in counts per seconds. The relative intensity of the peaks provides, through a linear relationship, the relative weight fraction for the different orientations.

grain orientation is uniformly distributed and in Fig. 7(b) the grain orientation is based on the XRD-measurements for poly-silicon deposited at 610 °C as reported in Table IV. Compared to the preferred orientation case, the uniform distribution gives a more uniform modulus distribution, although there is an increase in density around 170 GPa and a small decrease around 180 GPa. When the preferred orientation defined from the XRD measurements is taken into account, the histogram is drastically different. Although the whole spectrum is spanned (from 130 GPa to 188 GPa), very few samples are obtained in some regions and most of the samples are obtained either in a close



*Prepared using* nmeauth.cls
DOI: 10.1002/nme

Table IV. Percentage of the different grain orientations based on XRD measurements for the different temperatures of the fabrication process

| **Deposition temperature** [°C] | 580 | 610 | 630 | 650 |
|---|---|---|---|---|
| < **111** > | 12.57 | 19.96 | 12.88 | 11.72 |
| < **220** > | 7.19 | 13.67 | 7.96 | 7.59 |
| < **311** > | 42.83 | 28.83 | 39.08 | 38.47 |
| < **400** > | 4.28 | 5.54 | 3.13 | 3.93 |
| < **331** > | 17.97 | 18.14 | 21.32 | 20.45 |
| < **422** > | 15.15 | 13.86 | 15.63 | 17.84 |

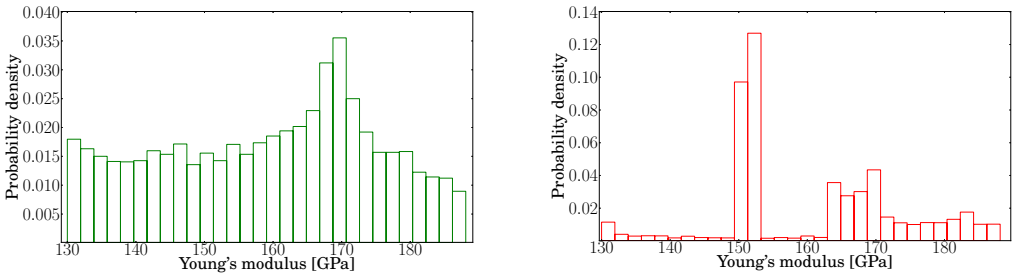


(a) Uniform distribution (b) Preferred orientation

Figure 7. Young's modulus for a silicon crystal whose orientation is (a) uniformly distributed, (b) preferentially distributed following Table IV at 610 °C

vicinity of $\approx$ 150 GPa or above $\approx$ 162 GPa. In terms of statistical moments, the means of the Young's modulus are respectively 159 GPa and 161.09 GPa for the uniform distribution and the preferred orientation cases. The standard deviations are respectively 15.76 GPa and 12.98 GPa for the uniform distribution and the preferred orientation cases. Although the two PDFs are drastically different, the first and second moments of their statistical behavior are similar.

The AFM measurements reported in Fig. 8(a) correspond to the sample processed with the deposition temperature of 610 °C. Five sets of AFM measurements are available; each with $1024 \times 1024$ sampling points of the surface height and with a spatial step along both $x$ and $y$



*Prepared using* nmeauth.cls DOI: 10.1002/nme

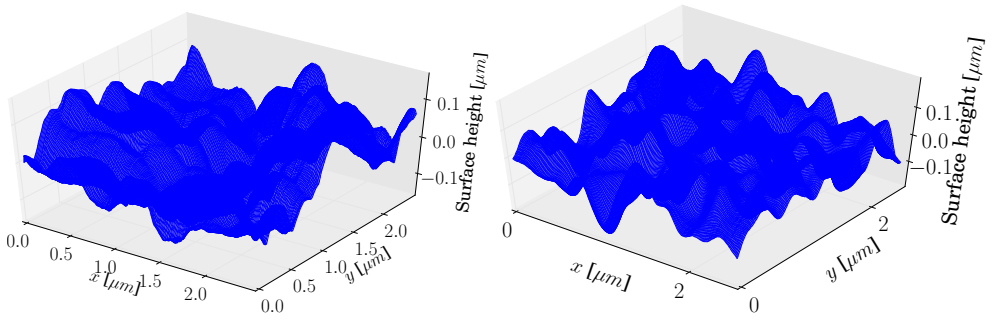


(a) AFM measurements (b) Generated surface

Figure 8. Sample of rough surfaces obtained with (a) AFM measurements on the poly-silicon deposited at 610 °C, and (b) the surface generator

directions of 4.883 $\mu$m. The height distribution shows a standard deviation of 60.3 nm for the deposition temperature of 610 °C, see Table V.

Table V. Standard deviation of the asperities height from AFM images and for the different temperatures of the fabrication process

| **Deposition temperature** [°C] | 580 | 610 | 630 | 650 |
|---|---|---|---|---|
| **Standard deviation of the asperities height** [nm] | 35.6 | 60.3 | 90.7 | 88.3 |

### *5.2. Generation of rough stochastic volume elements based on experimental measurements*

Two sources of uncertainties are considered on the meso-scale volume elements: on the one hand the material uncertainties such as the grain size and orientation distributions, and on the other hand the geometrical uncertainties resulting from the surface roughness.

The effect of the material uncertainties assuming a uniform orientation distribution was already studied in [1]. Results with a preferred orientation of grains based on XRD measurements are now considered: based on the measurements, some orientations are defined to be more likely than others. The effect of the preferred orientation on the results at both the meso-scale and macro-scale is discussed in the following sections. As it was shown in the previous subsection, the temperature considered during the deposition process has an effect on the micro-scale structure uncertainties.



*Prepared using* nmeauth.cls
DOI: 10.1002/nme

In order to illustrate how the developed 3-scale stochastic method can be used to propagated the uncertainties, we consider, as an example, the case of poly-silicon deposited at 610 °C. Moreover, although the experimental measurements were obtained for a poly-silicon thickness of 2 $\mu$m, in order to study the effect of the roughness for different MEMS thicknesses, we will consider that the measures remain valid for other thicknesses[**]

The second source of uncertainty, the roughness, is also considered in this section. As the grain distribution and the asperities are correlated, as shown in [38], both AFM and SEM measurements are used to generate samples of the RSVE structures. Indeed, as the asperities are normally formed on the top grains, the valleys of the surface topology thus being located at grain boundaries, both grain generation and roughness generation should be closely linked. This can be achieved in two ways: (i) either the grains are generated first and the surface is defined with respect to the grains, or (ii) the surface is generated first and the grains are defined with respect to the surface. With the former procedure, the grain centers define the position of the asperities but a lot of degrees of freedom still needs to be fixed (valley depth, peak high, ...) while respecting the surface properties (mean plane, RMS value, ...). The latter procedure is much easier to implement as follows. Once a correlation structure for the surface is defined (based on AFM measurements, grain size...), samples of the surface can be generated. The tips of the asperities for each surface can be detected and their positions used as seeds of a Voronoï tessellation to define the grains. The different steps of the meso-scale volume element generation, for both rough and flat SVEs, are discussed in the following sections.

*5.2.1. Asperities detection* The first step of the RSVE generation is to define an asperities detection process from the AFM images. In other words, from a surface sample obtained from AFM

[**]Measurements actually performed on 1 $\mu$m-thick poly-silicon films confirm that the main driving parameter is the deposition temperature. The main difference lies in the roughness. For example at a deposition temperature of 610 °C, the standard deviation of the height distribution decreases from 60.3 nm to 54.3 nm when the poly-silicon film thickness decreases from 2 to 1 $\mu$m, while for a deposition temperature of 580 °C, the standard deviation of the height distribution is around 35 nm.



*Prepared using* nmeauth.cls DOI: 10.1002/nme

measurements, the position of the local maxima must be found. The procedure defined in this work is a very simple one which requires smooth surfaces to provide relevant results. Each sample point of the surface of interest is analyzed. A point is considered to be the tip of one asperity if the following two conditions are respected simultaneously:

(i) It is the maximum value over its neighbors located in a square of diagonal length $L^1_{\text{lim}}$

(ii) There is no other asperity nearby located in a square of diagonal length $L^2_{\text{lim}}$

To illustrate the process, we consider the AFM measurements reported in Fig. 8(a), which correspond to the deposition temperature of 610 °C. The values of $L^1_{\text{lim}}$ and $L^2_{\text{lim}}$ are chosen to be $0.6\,\mu$m, as for the given smooth surfaces analyzed, these values provide relevant asperities. Applying the simple asperity detection method on these AFM measurements gives us an estimate of the grain size as each asperity is assimilated to one grain and as the area of each grain is $\pi\left(\frac{d}{2}\right)^2$, $d$ being the grain size. A computed grain size of $\approx 0.57\ \mu$m is obtained. There is a scatter between this value and the grain size $\approx 0.447\ \mu$m computed with the help of the SEM images, see Table II. The grain size resulting from the SEM images of $0.447\ \mu$m is thus enforced when generating the RSVEs in the following sections.

*5.2.2. Covariance structure of the rough surfaces* To generate the rough stochastic volume elements, the first thing that is created is their top rough surface. This is achieved using the spectral methods [45] with which a scalar value $h'$, the variation between the mean thickness and the local thickness, is generated over a 2D space. This process requires a 2D spatial covariance function $\bar{R}_{h'}(\boldsymbol{\tau})$ of $h'$, where $\boldsymbol{\tau}$ is the in-plane spatial vector between two points of interest. From the correlation function $R_{h'}(\boldsymbol{\tau}) = \frac{\bar{R}_{h'}(\boldsymbol{\tau})}{\sigma^2_{h'}}$ and the standard deviation $\sigma_{h'}$, $h'$ is generated as a stationary Gaussian random field using the theory reported in Section 4.2, but for a single variable $h'$.

As smooth surfaces must be considered for the asperity detection process, a Gaussian covariance function is assumed with

$$\bar{R}_{h'}(\tau) = \sigma^2_{h'} \exp^{-\frac{\tau^2\pi}{l^2_{h'}}}, \tag{81}$$



*Prepared using* nmeauth.cls
DOI: 10.1002/nme

where $\tau$ is the norm of the vector $\boldsymbol{\tau}$. This Gaussian covariance structure has two degrees of freedom: the standard deviation $\sigma_{h'}$ and the correlation length $l_{h'}$. The former value corresponds to the measured standard deviation obtained from the surface topology AFM measurements, and is evaluated as $\sigma_{h'} = 60.3$ nm.

The correlation length remains to be defined as it drives the distance between the asperities of the random field, thus enforcing the grain size. The grain size is a parameter of prime importance, not only concerning the roughness but also concerning the material property. The bigger the grain size, the higher the uncertainties at the meso-scale, as it was shown in [1] [††]. The correlation length $l_{h'}$ is computed so that the generated RSVEs possess an average grain size similar to the estimation of the SEM images, *i.e.* an average grain size of 0.447 $\mu$m for a deposition temperature of 610°C. This is achieved by defining an optimization procedure. From a first guess of the correlation length, surfaces can be generated and the corresponding grain size can be estimated. The correlation length is updated until the appropriate grain size is obtained. After computation, a value of $\frac{l_{h'}}{\sqrt{\pi}} = 0.03125\,\mu$m was obtained.

The resulting Gaussian covariance is depicted in Fig. 9(a), and is compared to the data computed from the AFM measurements in Fig. 9(b). As one can see in the picture, the experimental results do not converge for long distance as there were not enough sampling points. This justifies the use of a Gaussian correlation instead of the direct use of the AFM measurements. Let us note that keeping a spacing $\delta x$ of $4.883\,n$m, which is the spacing of the AFM measurements, is computationally expensive when volume elements of sizes around 1.0 $\mu$m must be generated. The Gaussian correlation assumption allows us to choose the spatial spacing and therefore a larger spacing of $10^{-2}$ $\mu$m is used.

Once the covariance structure is known, samples of the rough surfaces can be generated, and a sample of the surface is illustrated in Fig. 8(b).

[††]In [1], meso-scale uncertainties for different SVE sizes with a constant grain size was actually studied. Similar reasoning can however be obtained with a constant SVE size and different grain sizes



*Prepared using* nmeauth.cls DOI: 10.1002/nme

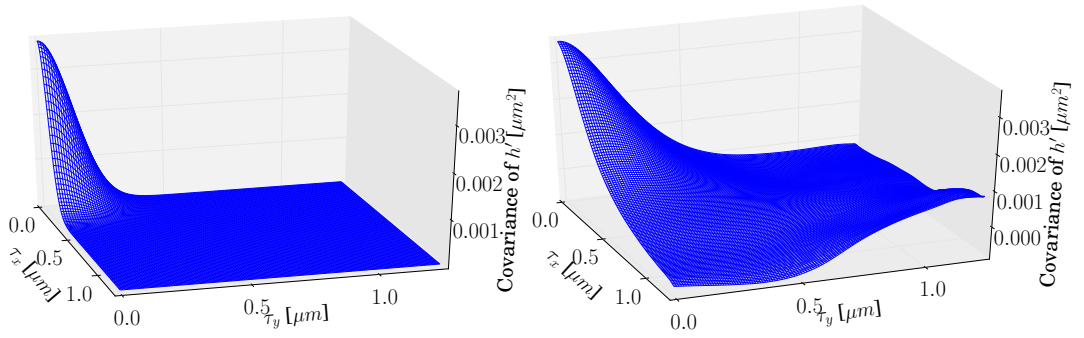


(a) Gaussian covariance (b) Covariance from AFM measurements

Figure 9. The covariance $\bar{R}_{h'}(\tau)$ of the surface height: (a) Gaussian covariance; and (b) from AFM measurements

*5.2.3. From the asperities to the RSVE meshes* Owing to the correlation between the rough surface and the grain structure, the Voronoï tessellation is generated based on the asperities information, with the seeds of the tessellation corresponding to the asperities of the surface. The Voronoï tessellation and its seeds, which correspond to the surface sample of Fig. 8(b), are depicted in Fig. 10(a). A columnar finite element mesh can then be extruded with the help of *gmsh* [60], and the position of each vertex of the mesh is then modified so that the top surface matches the rough surface illustrated in Fig. 8(b), leading to the finite element mesh reported in Fig. 10(b). At this point the polycrystalline material with its correlated roughness is then defined. As required for the computation of the homogenized material operators of the (R)SVEs, the desired output must be computed at different $x$ and $y$ locations of the micro-structure reported in Fig. 10(b), so that the spatial correlation can be captured using the moving-window technique detailed in [1] and illustrated in Fig. 3. A set of RSVEs is then extracted from the micro-structure using the moving-window technique following the schematics reported in Figs. 10(c)-10(d).

### *5.3. Stochastic homogenized meso-scale properties*

Using the (R)SVEs generated in the previous Section 5.2, stochastic homogenized properties can be computed thanks to the homogenization process described in Section 3. Thus the probabilistic



*Prepared using* nmeauth.cls DOI: 10.1002/nme

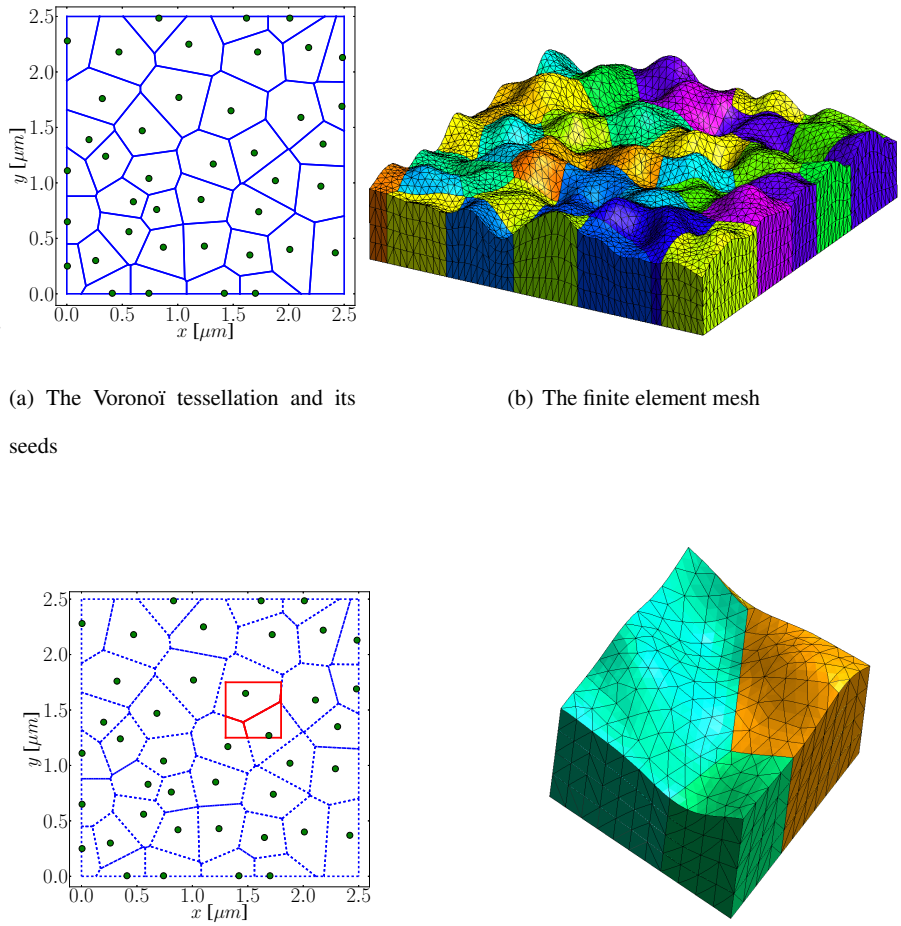


(a) The Voronoï tessellation and its seeds

(b) The finite element mesh

(c) A window in the tessellation

(d) The RSVE mesh

Figure 10. Generation of the RSVEs using the moving window-technique: (a) one sample of large Voronoï tessellation-based micro-structure, (b) the extruded finite element mesh of the large Voronoï tessellation, (c) one moving-window of the tessellation, and (d) the corresponding RSVE finite element mesh

material behavior at the meso-scale can be extracted from the (R)SVEs information, and because of the use of the moving-window technique the spatial correlation is captured as well. In terms of (R)SVE shape, only square-shaped (R)SVEs are generated. The (R)SVE length ranges between 0.5 $\mu$m to 1.5 $\mu$m and the thickness between 0.5 $\mu$m to 2 $\mu$m. Although the poly-silicon film statistical properties (grain size, roughness) can change with the deposition thickness, in order to separate and compare the different effects (material, surface roughness, and the MEMS thickness), we will assume identical statistical properties for the different MEMS thicknesses[**].



*Prepared using* nmeauth.cls
DOI: 10.1002/nme

The effects of different sources of uncertainties are investigated in this section. The name of the different uncertainty cases respects the following notation:

(i) The first letter, 'F' or 'R', refers to flat –*i.e.* without profile uncertainties– or rough SVEs;

1. Then the type of material is given, 'Si' refering to the anisotropic silicon and 'Iso' to a pseudo isotropic material;

(ii) Finally, two cases of grain orientation are considered: either uniform orientation distribution (subscript 'uni') or prefered XRD-based orientation (subscript 'pref').

The different cases are thus denoted by

(i) **Case F** – $\mathbf{Si_{uni}}$: Flat SVEs made of silicon with a uniform grain orientation distribution;

(ii) **Case F** – $\mathbf{Si_{pref}}$: Flat SVEs made of silicon whose grain orientation distribution is based on the XRD measurements;

(iii) **Case R** – **Iso**: RSVEs made of a pseudo isotropic material (160 GPa);

(iv) **Case R** – $\mathbf{Si_{uni}}$: RSVEs made of silicon with a uniform grain orientation distribution;

(v) **Case R** – $\mathbf{Si_{pref}}$: RSVEs made of silicon whose grain orientation distribution is based on the XRD measurements.

*5.3.1. Effect of the preferred grain orientation* The influence of the orientation is studied in Fig. 11, where the distribution of the homogenized meso-scale Young's modulus $E_x$, the Young's modulus along the $x$ direction, is reported for $0.5 \times 0.5 \times 0.5\,\mu\text{m}^3$ flat SVEs[‡‡]. 122 and 116 Voronoï tessellations were constructed respectively for the uniform grain orientation distribution and for the preferred grain orientation distribution, and 100 SVEs were extracted in each Voronoï tessellation following the moving-window technique. The average number of grains per SVE is $\approx 5.4$. In terms of statistical moments, the means of the Young's modulus are respectively 161.87 GPa and 162.09 GPa for the uniform orientation distribution and for the preferred orientation distribution, while their standard deviations are respectively 9.45 GPa and 8.01 GPa. Compared to the single

[‡‡]As we are considering the homogenized Young's modulus of flat SVEs, a first-order homogenization with Orthogonal Uniform Mixed Boundary Conditions, as detailed in [1], was considered in this Section 5.3.1



*Prepared using* nmeauth.cls DOI: 10.1002/nme

crystal case, see Fig. 7, the mean remains similar but the variance decreases after homogenization as expected. As it was already observed for the single crystal cases, the variance of $E_x$ decreases when the preferred orientation distribution is considered, although the PDFs are much more similar, and closer to a Gaussian distribution, than for the single crystal case.

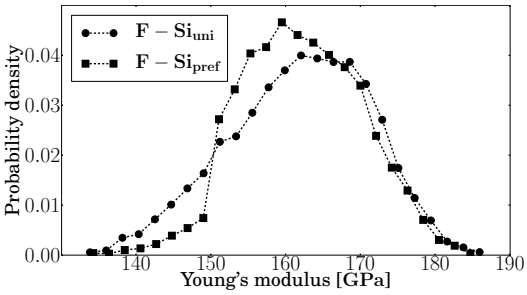


Figure 11. Distribution of the meso-scale Young 's modulus along the $x$-direction with and without preferred grain orientation for $0.5 \times 0.5 \times 0.5\ \mu\text{m}^3$ SVEs

*5.3.2. Effect of the surface topology* The effects of the roughness on the meso-scale mass per membrane unit area $\bar{\rho}$ and on the meso-scale material tensor $\boldsymbol{U}$ are now investigated. As in this paper the quantity of interest at the macro-scale is the beam resonance frequency, the element $\boldsymbol{U}^{(44)}$ of the meso-scale material tensor is the main focus as it links the bending stress and to the curvature.

At first, the probability density function of the mass per unit area $\bar{\rho}$ is illustrated in Fig. 12 where 65 500 RSVEs samples of size $0.5 \times 0.5 \times 0.5\ \mu\text{m}^3$ were considered.

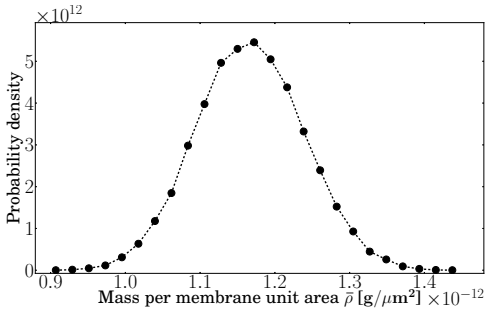


Figure 12. Distribution of the meso-scale mass per unit area $\bar{\rho}$ for $0.5 \times 0.5 \times 0.5\ \mu\text{m}^3$ RSVEs



*Prepared using* nmeauth.cls
DOI: 10.1002/nme

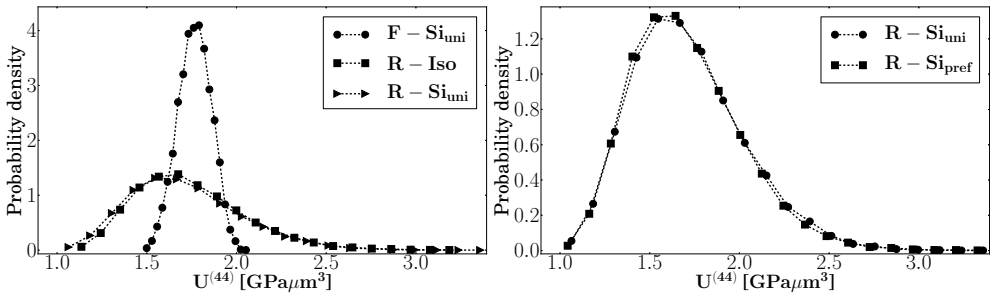


(a) Rough vs. flat SVEs (b) Grain orientation distribution effect

Figure 13. Distributions of the meso-scale $\boldsymbol{U}^{(44)}$ for different uncertainty cases with $0.5 \times 0.5 \times 0.5$ $\mu$m$^3$ (R)SVEs

The distribution of $\boldsymbol{U}^{(44)}$ is illustrated in Fig. 13 for a (R)SVE of size $0.5 \times 0.5 \times 0.5$ $\mu m^3$. In the case of RSVEs, the thickness size is actually the mean thickness $\bar{h}$ of the Voronoï tessellation. The different SVE cases are compared and it can be seen that the roughness is the main source of uncertainty. Indeed, while when considering the rough SVEs the PDFs are similar for the uniform grain orientation distribution and for the preferred grain orientation distribution, they are drastically different to the one obtained with flat SVEs. The statistical moments for the different cases are reported in Table VI. Finally, one can note that the distributions are not Gaussian thus showing the need for non-Gaussian stochastic models.

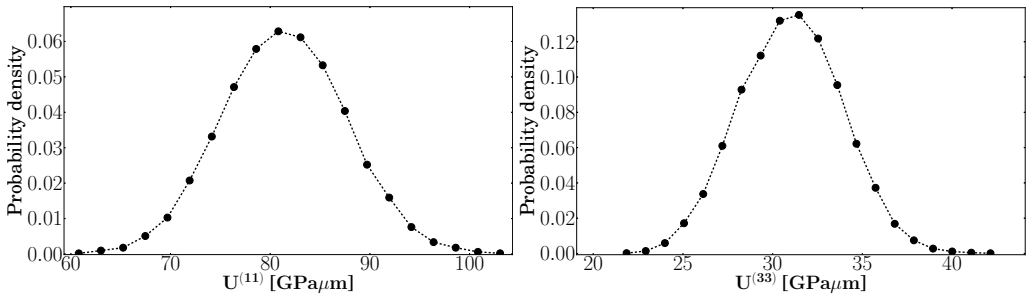


(a) $\boldsymbol{U}^{(11)}$ (b) $\boldsymbol{U}^{(33)}$

Figure 14. Distributions of the meso-scale fields (a) $\boldsymbol{U}^{(11)}$ and (b) $\boldsymbol{U}^{(33)}$ obtained for the particular R − Si$_{\text{pref}}$ case with RSVEs of dimension $0.5 \times 0.5 \times 0.5$ $\mu$m$^3$



*Prepared using* nmeauth.cls DOI: 10.1002/nme

Besides the bending properties, for completness the distribution of $\boldsymbol{U}^{(11)}$, which links the in-plane tension stress $\tilde{\boldsymbol{n}}_{xx}$ and strain $\boldsymbol{\upsilon}_{xx}$ can be seen in Fig. 14(a) for the particular $\mathrm{R}-\mathrm{Si}_{\mathrm{pref}}$ case. Moreover the distribution of $\boldsymbol{U}^{(33)}$, characterizing the response of the (R)SVEs to in-plane shearing, is illustrated in Fig. 14(b).

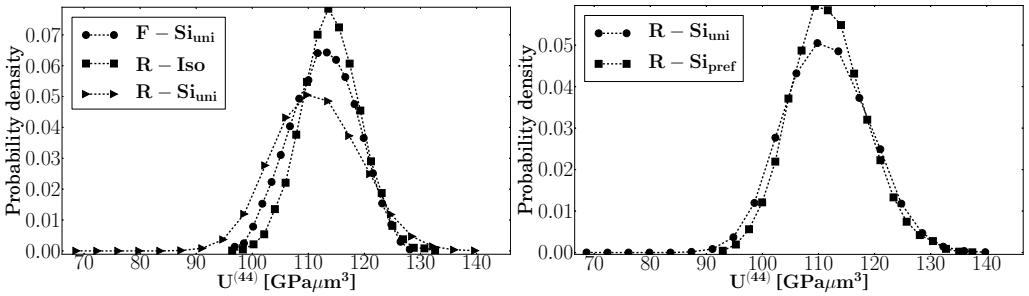


(a) Rough vs. flat SVEs (b) Grain orientation distribution effect

Figure 15. Distributions of the meso-scale $\boldsymbol{U}^{(44)}$ for different uncertainty cases with $0.5 \times 0.5 \times 2\ \mu\mathrm{m}^3$ (R)SVEs

However the importance of the roughness on the uncertainties tends to decrease when we consider thicker SVEs. Indeed, it can be seen in Figs. 15(a) and 15(b), in which the RSVEs mean thickness is $\bar{h} = 2\ \mu$m, that the material uncertainty resulting from the effect of the grain orientation distribution becomes comparable to the roughness effect.

*5.3.3. Effect of the RSVE length* The effect of the RSVE length on the meso-scale field $\boldsymbol{U}^{(44)}$ is illustrated in Fig. 16. Square-shaped RSVEs of successive lengths 0.5, 1.0, and 1.5 $\mu$m are considered.

The computed PDFs of $\boldsymbol{U}^{(44)}$ are shown in Fig. 16(a) for a 0.5 $\mu$m-thick RSVE, and the computed mean $\mathbb{E}[\boldsymbol{U}^{(44)}]$ and standard deviation $\sigma_{\boldsymbol{U}^{(44)}}$ are reported in Table VII. As expected, uncertainties decrease with the RSVE sizes. This can also be seen in Fig. 16(b) where the coefficient of variation of $\boldsymbol{U}^{(44)}$, $\mathrm{COV}_{\boldsymbol{U}^{(44)}} = \frac{\sigma_{\boldsymbol{U}^{(44)}}}{\mathbb{E}[\boldsymbol{U}^{(44)}]} \times 100\%$, is shown for different RSVE sizes and thicknesses.

*5.3.4. Spatial correlation* Owing to the moving-window technique used when extracting the RSVEs from the large Voronoï tesselations [1], the in-plane spatial (auto)-correlation $R_{\boldsymbol{U}^{(44)}}(\boldsymbol{\tau})$ of



*Prepared using* nmeauth.cls DOI: 10.1002/nme

Table VI. Statistical moments of $\boldsymbol{U}^{(44)}$ for the different meso-scale uncertainties cases. $N_{\text{Voronoï}}$ corresponds to the number of Voronoï tessellations generated. $N_{\text{window}}$ corresponds to the number of windows considered for each Voronoï tessellation to generate the $0.5 \times 0.5 \times 0.5\ \mu\text{m}^3$ (R)SVEs.

| **Cases** | $\mathbb{E}[\boldsymbol{U}^{(44)}]$ [GPa $\cdot\ \mu$m$^3$] | $\sigma_{\boldsymbol{U}^{(44)}}$ [GPa $\cdot\ \mu$m$^3$] | $N_{\text{Voronoï}}$ | $N_{\text{window}}$ |
|---|---|---|---|---|
| $\mathbf{F-Si_{uni}}$ | 1.77 | 0.092 | 149 | 100 |
| $\mathbf{F-Si_{pref}}$ | 1.78 | 0.068 | 162 | 100 |
| $\mathbf{R-Iso}$ | 1.74 | 0.306 | 136 | 100 |
| $\mathbf{R-Si_{uni}}$ | 1.71 | 0.312 | 201 | 100 |
| $\mathbf{R-Si_{pref}}$ | 1.70 | 0.306 | 258 | 100 |

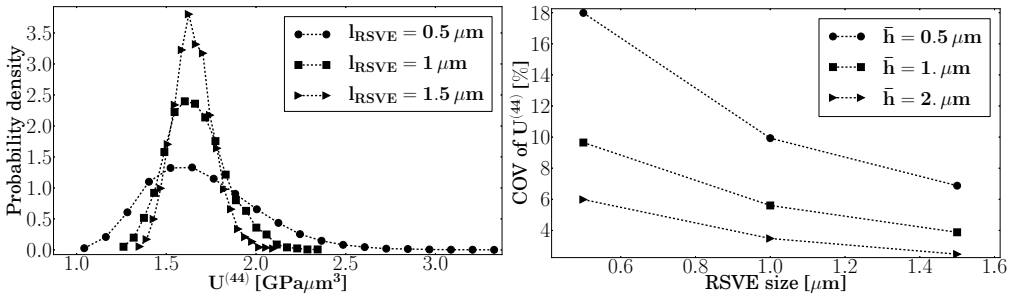


(a) Length effect (b) Length and thickness effects

Figure 16. Distributions of the meso-scale $\boldsymbol{U}^{(44)}$ for different RSVE sizes and for the particular $\text{R}-\text{Si}_{\text{pref}}$ case: (a) PDFs for RSVEs of lengths 0.5, 1.0, and 1.5 $\mu$m and of thickness 0.5 $\mu$m; and (b) coefficient of variations for different RSVEs lengths and thicknesses

$\boldsymbol{U}^{(44)}$ is directly available following

$$R_{\bullet}(\boldsymbol{\tau}) = \frac{\mathbb{E}\left[\left(\bullet(\mathbf{0}) - \mathbb{E}[\bullet]\right)\left(\bullet(\boldsymbol{\tau}) - \mathbb{E}[\bullet]\right)\right]}{\sigma_{\bullet}^2}, \tag{82}$$

where $\boldsymbol{\tau}$ is the in-plane vector separating two RSVE centers of a Voronoï tesselation, see Fig. 3, $\bullet$ is the field of interest, and $\sigma_{\bullet}$ is the standard deviation. The 2D in-plane spatial correlation is illustrated in Fig. 17(a) for a RSVE length of 0.5 $\mu$m, a RSVE mean thickness $\bar{h} = 0.5\ \mu m$, and for the particular $\text{R}-\text{Si}_{\text{pref}}$ case. Ten windows per direction (and per Voronoï tesselation) are



*Prepared using* nmeauth.cls DOI: 10.1002/nme

Table VII. Statistical moments of $\boldsymbol{U}^{(44)}$ for the different RSVE lengths, for a RSVE thickness of 0.5 $\mu$m, and for the particular R − $\text{Si}_{\text{pref}}$ case. $N_{\text{Voronoï}}$ corresponds to the number of Voronoï tessellations generated. $N_{\text{window}}$ corresponds to the number of windows considered for each Voronoï tessellation.

| $l_{\text{RSVE}}$ [$\mu$m] | $\mathbb{E}[\boldsymbol{U}^{(44)}]$ [GPa $\cdot$ $\mu$m$^3$] | $\sigma_{\boldsymbol{U}^{(44)}}$ [GPa $\cdot$ $\mu$m$^3$] | $N_{\text{Voronoï}}$ | $N_{\text{window}}$ |
|---|---|---|---|---|
| 0.5 | 1.70 | 0.312 | 258 | 100 |
| 1.0 | 1.67 | 0.165 | 202 | 36 |
| 1.5 | 1.65 | 0.114 | 191 | 25 |

considered, with a spacing along both $x$ and $y$ directions of 0.125 $\mu$m. The spatial correlation along the $x$-direction is illustrated in Fig. 17(b) for different RSVE lengths. These figures show that the correlation becomes close to zero for RSVE distances getting close to the RSVE length, as the windows are not overlapping each other anymore and thus share a reduced amount of grains.

The computed correlation lengths $l_{\boldsymbol{U}^{(44)}}$, with

$$l_{\bullet} = \frac{\int_{-\infty}^{\infty} R_{\bullet}(\boldsymbol{\tau}) d\boldsymbol{\tau}}{R_{\bullet}(\boldsymbol{0})}, \tag{83}$$

are reported in Table VIII.

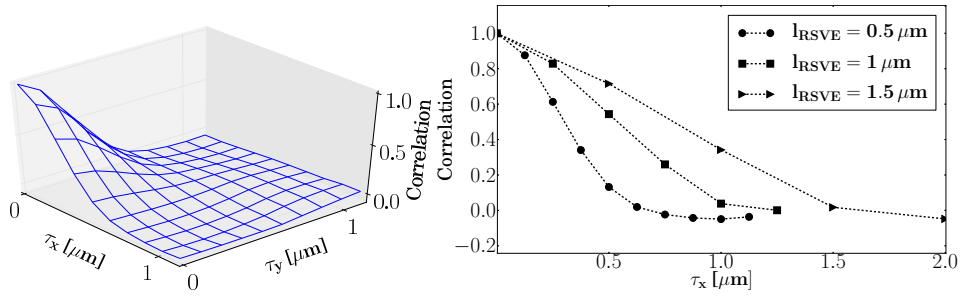


(a) 2D-spatial correlation (b) 1D-spatial correlation for different RSVE sizes

Figure 17. The spatial correlation of $\boldsymbol{U}^{(44)}$ for the particular R − $\text{Si}_{\text{pref}}$ case: (a) 2D-spatial correlation for RSVEs of size $0.5 \times 0.5 \times 0.5$ $\mu$m$^3$; and (b) spatial correlation along the $x$-direction for different RSVE lengths and for a RSVE thickness of 0.5 $\mu$m



*Prepared using* nmeauth.cls
DOI: 10.1002/nme

Table VIII. Correlation length $l_{\boldsymbol{U}^{(44)}}$ of $\boldsymbol{U}^{(44)}$ for different RSVE lengths for the particular $\mathrm{R}-\mathrm{Si}_{\mathrm{pref}}$ case and for a RSVE thickness of 0.5 $\mu$m

| $l_{\mathrm{RSVE}}$ [$\mu$m] | **Correlation length** $l_{\boldsymbol{U}^{(44)}}$ [$\mu$m] |
|---|---|
| 0.5 | 0.59 |
| 1.0 | 1.09 |
| 1.5 | 1.55 |

Finally, the cross-correlation between two fields $\bullet$ and $\star$ is also available using the moving-window technique, with

$$R^{\star}_{\bullet}(\boldsymbol{\tau}) = \frac{\mathbb{E}\left[\left(\bullet(\mathbf{0}) - \mathbb{E}\left[\bullet\right]\right)\left(\star(\boldsymbol{\tau}) - \mathbb{E}\left[\star\right]\right)\right]}{\sigma_{\bullet}\sigma_{\star}}\,. \tag{84}$$

The cross-correlations between different elements of the tangent $\boldsymbol{U}$ and $\bar{\rho}$ are shown in Fig. 18 for a separation $\boldsymbol{\tau} = \mathbf{0}$. In particular it can be seen that the meso-scale mass per unit area is strongly correlated to the entry of the meso-scale material tensor corresponding to the bending behavior as $R^{\bar{\rho}}_{\boldsymbol{U}^{(44)}}$ is higher than 0.8.

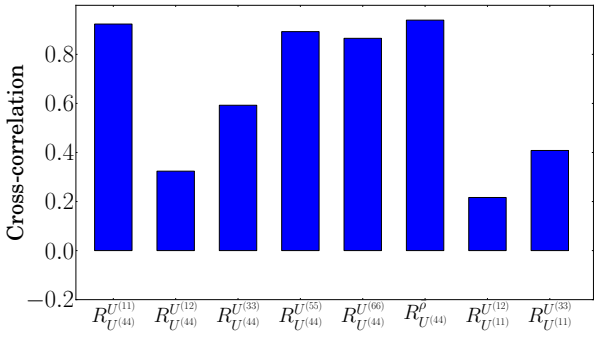


Figure 18. Cross-correlation between different elements of $\boldsymbol{U}$ and $\bar{\rho}$ for RSVEs of size $0.5 \times 0.5 \times 0.5$ $\mu$m$^3$ and for the particular $\mathrm{R}-\mathrm{Si}_{\mathrm{pref}}$ case

### *5.4. The random field generator*

The random field generator described in Section 4 is now applied to generate correlated fields for $\boldsymbol{U}$ and $\bar{\rho}$ based on the meso-scale properties previously computed in Section 5.3.



*Prepared using* nmeauth.cls
DOI: 10.1002/nme

At first, the zero-mean and unit variance variables $\boldsymbol{a}'$, which are actually considered by the stochastic model, are looked upon. The third and fourth order statistical moments, respectively $\gamma_{1_\bullet} = \frac{\mathbb{E}\left[(\bullet - \mathbb{E}[\bullet])^3\right]}{\sigma_\bullet^3}$ and $\beta_{2_\bullet} = \frac{\mathbb{E}\left[(\bullet - \mathbb{E}[\bullet])^4\right]}{\sigma_\bullet^4}$, of the those variables obtained from the (R)SVE resolutions are also studied and are found to be not always close to Gaussianity. For example, for RSVE dimensions of $0.5 \times 0.5 \times 0.5\ \mu\text{m}^3$ and for the particular R - $\text{Si}_{\text{uni}}$ case, out of the 22 variables, the furthest skewness from Gaussianity is $-1.172$, corresponding to the entry $\boldsymbol{a}'^{(8)}$ (a Gaussian variable being symmetric, its skewness is 0), and the furthest Kurtosis from Gaussianity is 5.104, also corresponding to the entry $\boldsymbol{a}^{(8)}$ (a Gaussian variable possessing a Kurtosis of 3). The distribution of $\boldsymbol{a}'^{(8)}$, obtained from the RSVE homogenization process, obtained using the Gaussian spectral generator, and obtained using the non-Gaussian mapping, can be seen in Fig. 19. The Gaussian spectral generator does not converge towards the micro-samples distribution, due to the higher moments of the distribution. This motivates the recourse to the non-Gaussian generator, as described in Section 4, whose results depicted in Fig. 19 are closer in terms of probability distribution to the micro-samples distribution than the Gaussian distribution. Indeed the skewness of the non-Gaussian generated mapping $\boldsymbol{a}'^{(8)}$ is $\gamma_{1_{\boldsymbol{a}'^{(8)}}} = -1.197$ and its Kurtosis is $\beta_{2_{\boldsymbol{a}'^{(8)}}} = 5.205$, in good agreement with the original inputs of the random field generator.

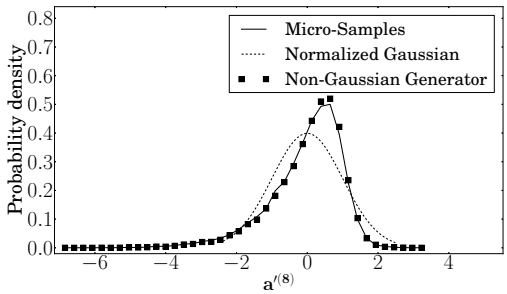


Figure 19. Computed and generated values of $\boldsymbol{a}'^{(8)}$ for RSVE dimensions of $0.5 \times 0.5 \times 0.5\ \mu\text{m}^3$ and for the particular R - $\text{Si}_{\text{uni}}$ case (Continuous curve: distribution obtained from the RSVE homogenization process; Dashed curve: normalized Gaussian distribution; Squares: non-Gaussian mapping)

The accuracy of the non-Gaussian generator is now assessed by comparing the generated values of interest $\boldsymbol{U}$ and $\bar{\rho}$ to the ones resulting from the RSVEs homogenization process. RSVE dimensions



*Prepared using* nmeauth.cls
DOI: 10.1002/nme

Table IX. Mean values of the PDFs obtained from the micro-samples and from the generated random fields (non-Gaussian) for RSVE dimensions of $0.5 \times 0.5 \times 0.5\ \mu\text{m}^3$ and for the particular R - $\text{Si}_{\text{pref}}$ case

| | **Micro-Samples** | **NG-Generator** |
|---|---|---|
| $\mathbb{E}\left[\boldsymbol{U}^{(11)}\right]$ [GPa $\cdot\ \mu$m] | 81.41 | 81.38 |
| $\mathbb{E}\left[\boldsymbol{U}^{(12)}\right]$ [GPa $\cdot\ \mu$m] | 16.85 | 16.84 |
| $\mathbb{E}\left[\boldsymbol{U}^{(33)}\right]$ [GPa $\cdot\ \mu$m] | 31.02 | 30.97 |
| $\mathbb{E}\left[\boldsymbol{U}^{(44)}\right]$ [GPa $\cdot\ \mu\text{m}^3$] | 1.70 | 1.69 |
| $\mathbb{E}\left[\boldsymbol{U}^{(53)}\right]$ [GPa $\cdot\ \mu\text{m}^2$] | $-0.025$ | $-0.026$ |
| $\mathbb{E}[\bar{\rho}]$ [g/$\mu\text{m}^2$] | $1.1635\,10^{-12}$ | $1.1624\,10^{-12}$ |

Table X. Standard deviation values of the PDFs obtained from the micro-samples and from the generated random fields (non-Gaussian) for RSVE dimensions of $0.5 \times 0.5 \times 0.5\ \mu\text{m}^3$ and for the particular R - $\text{Si}_{\text{pref}}$ case

| | **Micro-Samples** | **NG-Generator** |
|---|---|---|
| $\sigma_{\boldsymbol{U}^{(11)}}$ [GPa $\cdot\ \mu$m] | 6.18 | 5.92 |
| $\sigma_{\boldsymbol{U}^{(12)}}$ [GPa $\cdot\ \mu$m] | 2.86 | 2.68 |
| $\sigma_{\boldsymbol{U}^{(33)}}$ [GPa $\cdot\ \mu$m] | 2.83 | 2.66 |
| $\sigma_{\boldsymbol{U}^{(44)}}$ [GPa $\cdot\ \mu\text{m}^3$] | 0.31 | 0.29 |
| $\sigma_{\boldsymbol{U}^{(53)}}$ [GPa $\cdot\ \mu\text{m}^2$] | 0.12 | 0.12 |
| $\sigma_{\bar{\rho}}$ [g/$\mu\text{m}^2$] | $7.16\,10^{-14}$ | $6.81\,10^{-14}$ |

of $0.5 \times 0.5 \times 0.5\ \mu\text{m}^3$ and the particular R - $\text{Si}_{\text{pref}}$ case are considered. The probability distribution functions obtained directly from the RSVEs homogenization are compared to the non-Gaussian generated fields in Fig. 20 for different entries of $\boldsymbol{U}$ and $\bar{\rho}$. The generated field distributions are in good agreement with the distributions directly obtained from the micro-samples, although the spectral density of entries $\boldsymbol{U}$ obtained from the non-Gaussian generator slightly differs from the original ones, as $\boldsymbol{U}$ results from several entries of $\boldsymbol{a}'$ which is the originally treated value. However



*Prepared using* nmeauth.cls
DOI: 10.1002/nme

Table XI. Skewness values of the PDFs obtained from the micro-samples and from the generated random fields (non-Gaussian) for RSVE dimensions of $0.5 \times 0.5 \times 0.5\ \mu\text{m}^3$ and for the particular R - $\text{Si}_{\text{pref}}$ case

| | **Micro-Samples** | **NG-Generator** |
|---|---|---|
| $\gamma_{1\boldsymbol{U}^{(11)}}$ | 0.042 | 0.046 |
| $\gamma_{1\boldsymbol{U}^{(12)}}$ | $-0.27$ | $-0.24$ |
| $\gamma_{1\boldsymbol{U}^{(33)}}$ | 0.05 | 0.11 |
| $\gamma_{1\boldsymbol{U}^{(44)}}$ | 0.73 | 0.62 |
| $\gamma_{1\boldsymbol{U}^{(53)}}$ | 0.015 | $-0.002$ |
| $\gamma_{1\bar{\rho}}$ | 0.032 | 0.046 |

Table XII. Kurtosis values of the PDFs obtained from the micro-samples and from the generated random fields (non-Gaussian) with (R)SVE dimensions of $0.5 \times 0.5 \times 0.5\ \mu\text{m}^3$ for RSVE dimensions of $0.5 \times 0.5 \times 0.5\ \mu\text{m}^3$ and for the particular R - $\text{Si}_{\text{pref}}$ case

| | **Micro-Samples** | **NG-Generator** |
|---|---|---|
| $\beta_{2\boldsymbol{U}^{(11)}}$ | 2.97 | 2.97 |
| $\beta_{2\boldsymbol{U}^{(12)}}$ | 3.08 | 3.07 |
| $\beta_{2\boldsymbol{U}^{(33)}}$ | 2.83 | 2.91 |
| $\beta_{2\boldsymbol{U}^{(44)}}$ | 3.80 | 3.55 |
| $\beta_{2\boldsymbol{U}^{(53)}}$ | 3.86 | 3.73 |
| $\beta_{2\bar{\rho}}$ | 2.97 | 2.92 |

the accuracy of the non-Gaussian generator is confirmed by comparing the mean, standard deviation, skewness, and kurtosis, of the distributions obtained from the micro-samples and the non-Gaussian (NG) generator, which are respectively reported in Tables IX, X, XI, and XII.

The last properties whose accuracy has to be assessed are the spatial correlation and cross-correlation for $\boldsymbol{U}$ and $\bar{\rho}$. The 2D in-plane (auto)-correlation of $\boldsymbol{U}^{(44)}$ resulting from the random field generated by the stochastic model is compared to the spatial distribution obtained after performing



*Prepared using* nmeauth.cls
DOI: 10.1002/nme

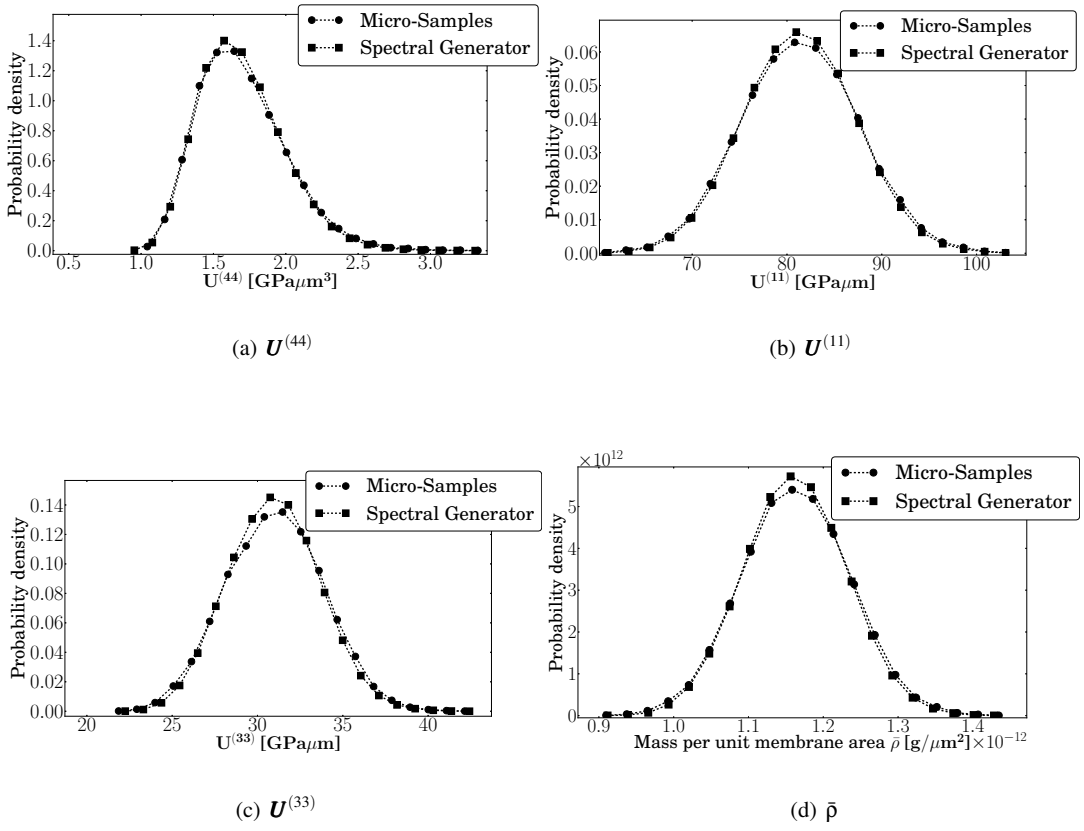


(a) $\boldsymbol{U}^{(44)}$ (b) $\boldsymbol{U}^{(11)}$

(c) $\boldsymbol{U}^{(33)}$ (d) $\bar{\rho}$

Figure 20. Comparison of different computed and generated meso-scale PDFs obtained for RSVE dimensions of $0.5 \times 0.5 \times 0.5\ \mu\text{m}^3$ and for the particular R - $\text{Si}_{\text{pref}}$ case

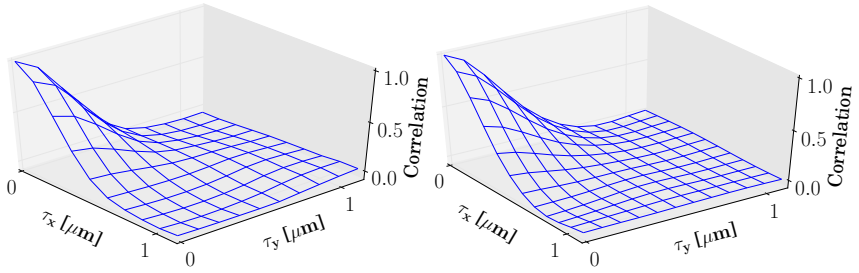


(a) Micro-Samples (b) Spectral Generator

Figure 21. Comparison of the 2D spatial (auto-)correlations of $\boldsymbol{U}^{(44)}$ obtained from the RSVE homogenization and from the generator (non-Gaussian mapping) for RSVE dimensions of $0.5 \times 0.5 \times 0.5\ \mu\text{m}^3$ and for the particular R - $\text{Si}_{\text{pref}}$ case



*Prepared using* nmeauth.cls
DOI: 10.1002/nme

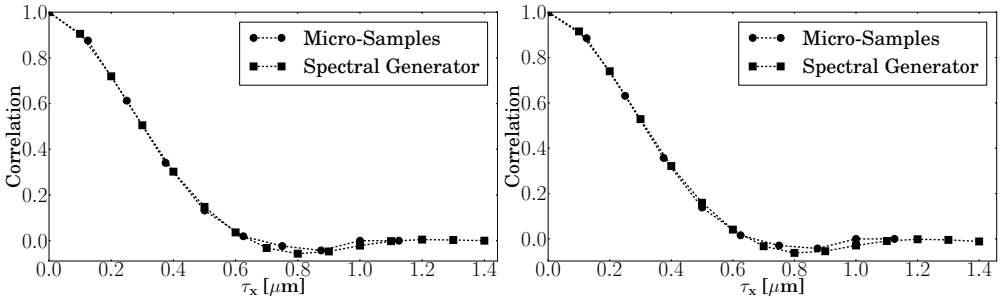


(a) $\boldsymbol{U}^{(44)}$ (b) $\boldsymbol{U}^{(11)}$

Figure 22. Comparison of the 1D spatial (auto-)correlations of (a) $\boldsymbol{U}^{(44)}$ and (b) $\boldsymbol{U}^{(11)}$ obtained from the RSVE homogenization and from the generator (non-Gaussian mapping) for RSVE dimensions of $0.5 \times 0.5 \times 0.5\ \mu\text{m}^3$ and for the particular R - $\text{Si}_{\text{pref}}$ case

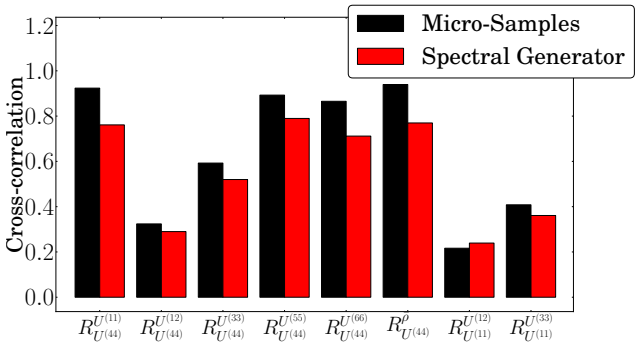


Figure 23. Comparison of the cross-correlations between different elements of $\boldsymbol{U}$ and $\bar{\rho}$ obtained from the RSVE homogenization and from the generator (non-Gaussian mapping) for RSVE dimensions of $0.5 \times 0.5 \times 0.5\ \mu\text{m}^3$ and for the particular R - $\text{Si}_{\text{pref}}$ case

the homogeneization process on the RSVEs in Fig. 21. Similarly, the 1D spatial correlation along the RSVE length for $\boldsymbol{U}^{(44)}$ and $\boldsymbol{U}^{(11)}$, obtained from the micro-samples and from the random field generator, are respectively illustrated in Figs. 22(a) and 22(b). It appears that the spatial auto-correlation is reproduced with accuracy by the generator. Finally, the cross-correlations resulting from the homogenization process and from the generated random field for different entries of $\boldsymbol{U}$ and $\bar{\rho}$ are compared in Fig. 23. Although some differences can be seen in the cross-correlation, the accuracy remains satisfying to generate results at the macro-scale.



*Prepared using* nmeauth.cls DOI: 10.1002/nme

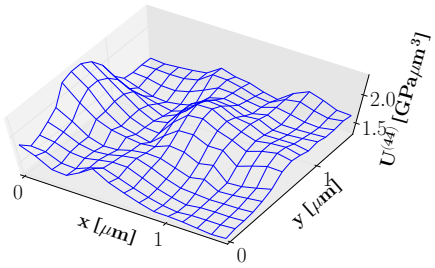


Figure 24. A sample of the generated field $\boldsymbol{U}^{(44)}$ for RSVE dimensions of $0.5 \times 0.5 \times 0.5\ \mu\text{m}^3$ and for the particular $R - Si_{prev}$ case

As a way of illustration, one realization of the random field entry $\boldsymbol{U}^{(44)}$ can be seen in Fig. 24.

### *5.5. Macro-scale SFEM*

Using the random fields generated in Section 5.4, macro-scale stochastic plate finite elements as defined in Section 2 are used on the basis of a Monte-Carlo procedure. At each spatial position $\boldsymbol{x}$, the spectral generator defined in Section 4 and illustrated in Section 5.4 is used to obtain realizations of the resultant meso-scale material tensor $U(\boldsymbol{x}, \boldsymbol{\theta})$ and of the meso-scale mass per membrane unit area $\bar{\rho}(\boldsymbol{x}, \boldsymbol{\theta})$. The spectral generator is based on the micro-samples obtained using the second-order computational homogenization process described in Section 3 and performed on the (R)SVEs generated from the measurements as discussed in Section 5.2.

*5.5.1. The problem definition* The spatial positions $\boldsymbol{x}$ of interest are defined based on the macro-scale mesh of the plate. Such a mesh, made of quadrangle plate elements, is depicted in Fig. 25 along with the corresponding integration points. Because of the use of the Continuous/Discontinuous Galerkin method, interface elements, with their integration points, are also required to integrate the interface contributions. The ghost elements, located outside the plate, are required to model the clamping of the plate, by enforcing weakly a zero out-of-plane displacement derivative. Bi-quadratic shape functions are considered for plate elements and quadratic shape functions are considered at the interfaces to enforce weakly the continuity of the out-of-plane displacement derivative.



*Prepared using* nmeauth.cls
DOI: 10.1002/nme

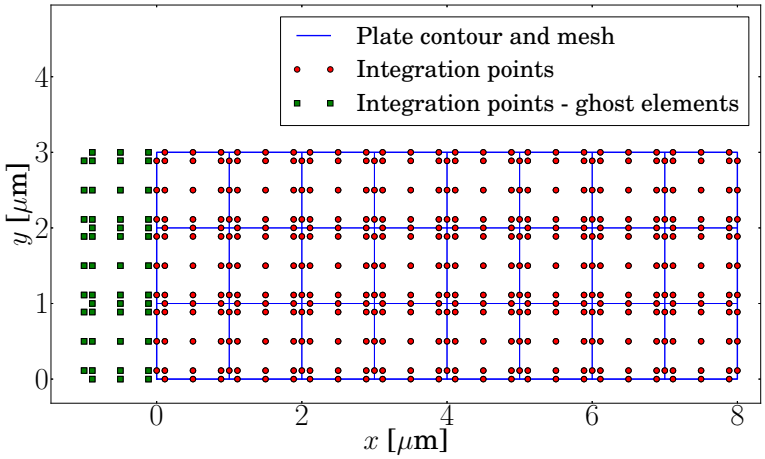


Figure 25. One macro-scale mesh with the corresponding integration points for a plate of dimension $8 \times 3\ \mu\text{m}^2$

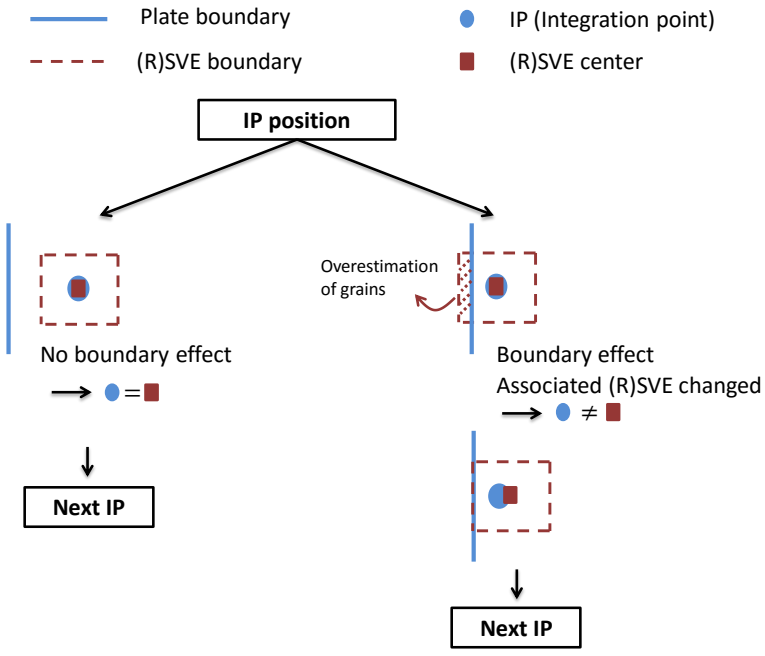


Figure 26. The boundary effect and its avoidance

A generated random field is thus evaluated at the different positions of the Gauss Integration Points (IP) in order to define the SFEM problem. However care must be taken of two aspects:



*Prepared using* nmeauth.cls
DOI: 10.1002/nme

(i) When generating the random field, one approximation results from the bi-linear interpolation used to retrieve the values at a desired $\boldsymbol{x}$ position (positions of the integration points defined by the macro-scale SFEM) from the values generated at *a priori* $\boldsymbol{x}'$ position obtained using the FFT approach (regular spacing).

(ii) A boundary effect exists when an integration point is located at the vicinity of the boundary of the plate: the heterogeneities number can then be overestimated as the centered (R)SVE has part of his domain outside of the macro-scale mesh as illustrated in Fig. 26. To circumvent this issue, the associated (R)SVE center is moved inward the plate to capture the right amount of heterogeneities as described in Fig. 26. Other discretization methods of the random fields such as the local average one could also be applied.

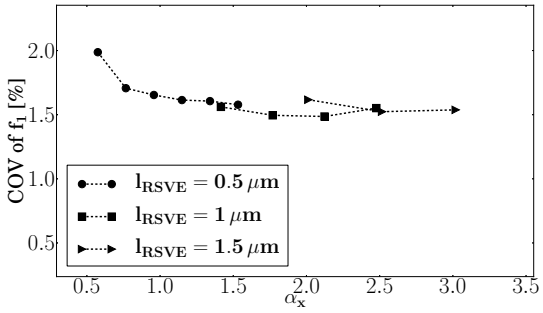


Figure 27. COV for different mesh sizes and RSVE lengths of the first mode frequency for a $16 \times 2 \times 0.5\,\mu m^3$ rectangular plate considering RSVE dimensions of $0.5 \times 0.5 \times 0.5\,\mu m^3$ and the R - $Si_{pref}$ case

As it was numerically verified by direct numerical simulations with a discretization of the micro-structure of MEMS resonator in [1], the stochastic multi-scale approach provides relevant results if the maximum distance $l_{IP}^{max}$ between the Integration Gauss Points (IP) of the macro-scale mesh is smaller than the correlation length $l_{\boldsymbol{U}\tilde{\rho}}$ (83) of the meso-scale random fields, which in turn depends on the (R)SVE size. The ratio $\alpha_i$ is thus defined, along the direction $i$, as:

$$\alpha_i = \frac{l_{\boldsymbol{U}\tilde{\rho}_i}}{l_{IP}^{max}{}_i}. \tag{85}$$

If the ratio $\alpha_i$ is smaller than 1, the uncertainty effects are overestimated as not enough heterogeneities are considered per integration point. Relevant results can only be obtained if $\alpha_i > 1$



*Prepared using* nmeauth.cls
DOI: 10.1002/nme

for each direction $i$. As the problem is herein mainly governed by $\boldsymbol{U}^{(44)}$, we define $\alpha_i > 1$ using the correlation length $l_{\boldsymbol{U}^{(44)}}$.

The convergence of the method with respect to $\alpha_x$ is shown in Fig. 27, for a $16 \times 2 \times 0.5\ \mu\text{m}^3$ rectangular plate, and for the $\text{R} - \text{Si}_{\text{pref}}$ case. The three different RSVE sizes studied at the meso-scale in Section 5.3 are considered: 0.5, 1.0, and 1.5 $\mu$m. Furthermore, different macro-scale mesh discretizations are considered. As the main direction of interest for this case of application is the plate length, the number of mesh elements along the $x$-direction is not constant, but the the mesh size along the $y$-direction does not change accordingly. The corresponding $\alpha_y$ parameters for each SVE size, 0.5, 1.0, and 1.5 $\mu$m, are respectively 2.3, 4.25, and 6.04, except for the two finest meshes of the 0.5 $\mu$m SVEs for which we have added a last finite element along the $y$-direction. As it can be seen on Fig. 27, the results converge toward a COV of about 1.5% for $\alpha_x > 1$. The difference of convergence point between the curves results, on the one hand from the constant and different values of $\alpha_y$, which cannot evolve with $\alpha_x$ because of mesh discretization constraints, and on the other hand from the boundary effect correction.

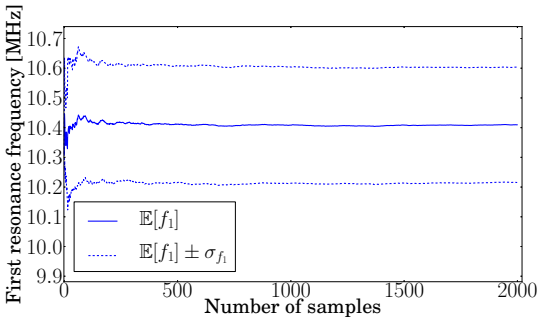


Figure 28. Convergence of the first mode frequency distribution for a $8 \times 3 \times 0.5\ \mu\text{m}^3$ rectangular plate considering RSVE dimensions of $0.5 \times 0.5 \times 0.5\ \mu\text{m}^3$ and the $\text{R} - \text{Si}_{\text{pref}}$ case

Once the macro-scale plate finite element problem has been defined, in order to conduct the probabilistic study, the number of realizations that has to solved should be defined. As the Monte Carlo simulation method is considered, for each macro-scale plate finite element realization, one random field is generated. Because of the existence of the random field generator and because of



*Prepared using* nmeauth.cls
DOI: 10.1002/nme

the reduced cost of the plate finite element model, the Monte Carlo simulation method is actually an efficient tool. To define the number of realizations, the convergence of the distribution of the first bending mode frequency $f_1$ is studied in Fig. 28 for a $8 \times 3 \times 0.5\ \mu\text{m}^3$ rectangular plate. The uncertainty case involved is the $\text{R} - \text{Si}_{\text{pref}}$ case, and the RSVE dimensions are $0.5 \times 0.5 \times 0.5\ \mu\text{m}^3$. The results have converged for 2000 samples, which is the number of realizations that will be considered in this section.

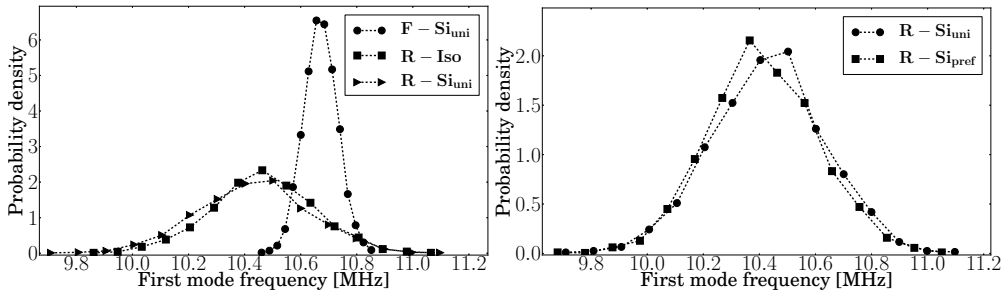


(a) Effect of roughness for $8 \times 3 \times 0.5\ \mu\text{m}^3$ plates (b) Effect of orientation for $8 \times 3 \times 0.5\ \mu\text{m}^3$ plates

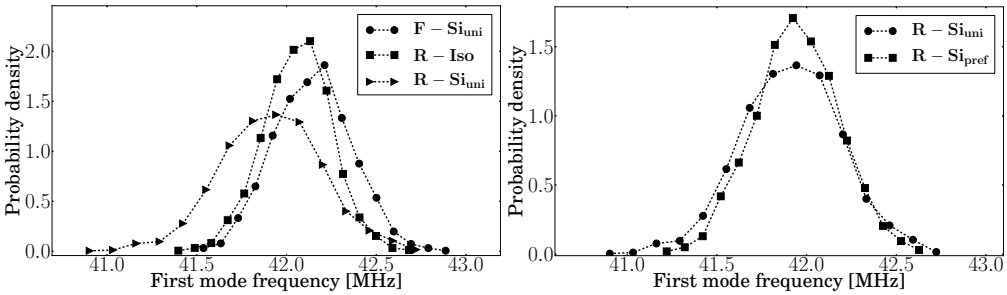


(c) Effect of roughness for $8 \times 3 \times 2\ \mu\text{m}^3$ plates (d) Effect of orientation for $8 \times 3 \times 2\ \mu\text{m}^3$ plates

Figure 29. The distribution of the resonance frequency of (a and b) $8 \times 3 \times 0.5\ \mu\text{m}^3$ plates, and of (c and d) $8 \times 3 \times 2\ \mu\text{m}^3$ plates for the different uncertainty cases

*5.5.2. The macro-scale effect of the different sources of uncertainties* The method is now used to study the effect of the different uncertainty cases, described in Section 5.3, on the plate behavior. In particular the first resonance frequency of $8 \times 3\ \mu\text{m}^2$ rectangular plates subjected to different cases of uncertainty is studied for two different thicknesses of $0.5\ \mu$m and $2\ \mu$m. The RSVE length



*Prepared using* nmeauth.cls DOI: 10.1002/nme

is 0.5 $\mu$m. For the 2 $\mu$m-thick plates, the Kirchhoff-Love assumption induces a bias in the average eigen frequency. However we consider this case as it allows comparing the effect of the roughness on the uncertainties for different thicknesses under the same modeling assumption.

The estimated probability density functions are depicted in Fig. 29 for the average plate thicknesses of $\bar{h} = 0.5$ $\mu$m and $\bar{h} = 2$ $\mu$m. The corresponding mean and standard deviation are given in Table XIII. In agreement with the results provided in Section 5.3, Table XIII and Fig. 29 show that the main source of uncertainty changes with the thickness of the plate. For a 0.5 $\mu$m-thick plate, the main source of uncertainty is due to the roughness, while for 2 $\mu$m-thick plate, the two sources of uncertainty (material and roughness) become of comparable effects.

Table XIII. Statistical moments of the first resonance frequency of $8 \times 3$ $\mu$m$^2$ rectangular plates for the different meso-scale uncertainties cases

| **Cases** | $\bar{\mathbf{h}} = \mathbf{0.5}\,\mu\mathbf{m}$ | | $\bar{\mathbf{h}} = \mathbf{2}\,\mu\mathbf{m}$ | |
|---|---|---|---|---|
| | $\mathbb{E}[f_1]$ [MHz] | $\boldsymbol{\sigma}_{f_1}$ [MHz] | $\mathbb{E}[f_1]$ [MHz] | $\boldsymbol{\sigma}_{f_1}$ [MHz] |
| $\mathbf{F-Si_{uni}}$ | 10.67 | 0.060 | 42.15 | 0.215 |
| $\mathbf{F-Si_{pref}}$ | 10.70 | 0.045 | 42.26 | 0.162 |
| $\mathbf{R-Iso}$ | 10.46 | 0.181 | 42.06 | 0.187 |
| $\mathbf{R-Si_{uni}}$ | 10.43 | 0.199 | 41.91 | 0.278 |
| $\mathbf{R-Si_{pref}}$ | 10.41 | 0.194 | 41.94 | 0.236 |

*5.5.3. The effect of the plate dimensions* The effect of the plate dimension is studied for the $\mathrm{R-Si_{pref}}$ uncertainty case and for 0.5 $\mu$m-long RSVEs in Fig. 30. Results obtained for different plate thicknesses are shown in Fig. 30(a). As expected, uncertainties decrease with the increase of the thickness of the plate as the roughness effect becomes less important. Changing the width has a large impact on the uncertainty as shown in Fig. 30(b): the larger the plate, the lower the uncertainties as the heterogeneities have less effects. Finally, results obtained for different lengths of the plate are shown in Fig. 30(c), where it can be seen that the uncertainty of the resonance



*Prepared using* nmeauth.cls DOI: 10.1002/nme

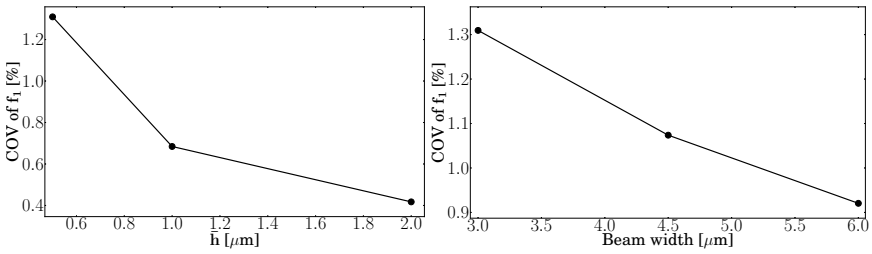


(a) Effect of the thickness

(b) Effect of the width

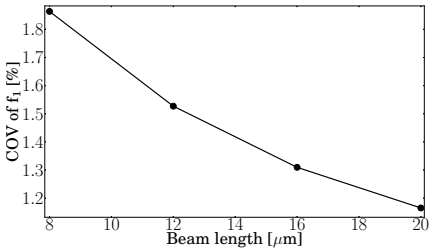


(c) Effect of the length

Figure 30. The effect of the plate dimensions on the first resonance frequency distribution for the $R - Si_{pref}$ case (a) for a 16 $\mu$m-long, 3 $\mu$m-wide plate and for different thicknesses, (b) for a 16 $\mu$m-long, 0.5 $\mu$m-thick plate and for different widths, and (c) for a 3 $\mu$m-wide, 0.5 $\mu$m-thick plate and for different lengths

frequency decreases with the length of the plate. However, considering a more realistic anchor of the MEMS than a perfect clamp, as done in [37], could change this conclusion.

Finally, the first two statistical moments obtained for different plate dimensions are gathered in Table XIV.

### *5.6. Computational efficiency*

With the developed stochastic multi-scale model, the computation cost is divided in several stages:

(i) The generation of the meshes of the RSVEs (including the generation of the rough surface), defined by given in-plane dimensions, one thickness, and one deposition temperature, and extracted using the moving-window technique, see Section 5.2, requires a computation time



*Prepared using* nmeauth.cls
DOI: 10.1002/nme

Table XIV. Statistical moments of the plate first resonance frequency for the different plate dimensions for the $\mathrm{R}-\mathrm{Si}_{\mathrm{pref}}$ case

| **Membrane geometry** | $\mathbb{E}[f_1]$ [MHz] | | |
|---|---|---|---|
| | $\bar{\mathbf{h}} = \mathbf{0.5}\ \mu\mathbf{m}$ | $\bar{\mathbf{h}} = \mathbf{1}\ \mu\mathbf{m}$ | $\bar{\mathbf{h}} = \mathbf{2}\ \mu\mathbf{m}$ |
| $\mathbf{8 \times 3}\ \mu\mathbf{m}^2$ | 10.41 | 20.98 | 41.94 |
| $\mathbf{8 \times 6}\ \mu\mathbf{m}^2$ | 10.46 | 21.06 | 42.11 |
| $\mathbf{16 \times 3}\ \mu\mathbf{m}^2$ | 2.58 | 5.22 | 10.50 |
| $\mathbf{16 \times 6}\ \mu\mathbf{m}^2$ | 2.59 | 5.24 | 10.54 |
| **Membrane geometry** | $\sigma_{f_1}$ [MHz] | | |
| | $\bar{\mathbf{h}} = \mathbf{0.5}\ \mu\mathbf{m}$ | $\bar{\mathbf{h}} = \mathbf{1}\ \mu\mathbf{m}$ | $\bar{\mathbf{h}} = \mathbf{2}\ \mu\mathbf{m}$ |
| $\mathbf{8 \times 3}\ \mu\mathbf{m}^2$ | 0.194 | 0.205 | 0.236 |
| $\mathbf{8 \times 6}\ \mu\mathbf{m}^2$ | 0.134 | 0.139 | 0.166 |
| $\mathbf{16 \times 3}\ \mu\mathbf{m}^2$ | 0.0338 | 0.0357 | 0.0438 |
| $\mathbf{16 \times 6}\ \mu\mathbf{m}^2$ | 0.0239 | 0.0252 | 0.0297 |

of a few minutes for 100 $0.5 \times 0.5 \times 0.5\ \mu\mathrm{m}^3$-RSVEs extracted from one tessellation, using a Python environment on a 2.1 GHz CPU;

(ii) The second-order computational homogenization of a $0.5 \times 0.5 \times 0.5\ \mu\mathrm{m}^3$-RSVE requires about 30 s, using a C++ environment on a 2.1 GHz CPU, so the computational time requires to perform 100 (windows per tessellation) homogenization resolutions, see Section 5.3, is about 1 hour. Note that about two hundreds tessellations are required to define the meso-scale random fields, but the computation related to the 200 tessellations, steps (i) and (ii), can be performed on several processors in a straightforward way as the tessellations are independent from each other.

(iii) The definition of the non-Gaussian stochastic model from the 200 (tessellations) times 100 (RSVEs per tessellation) homogenized properties, see Section 5.4, requires about 10 minutes



*Prepared using* nmeauth.cls DOI: 10.1002/nme

per iteration, using a Python environment on a 2.1 GHz CPU. For the $0.5 \times 0.5 \times 0.5$ $\mu$m$^3$-RSVEs, about 10 iterations are required, leading to a couple of hours of computation time.

(iv) The resolution of the macro-scale SFEM, see Section 5.5, requires a few seconds to generate one meso-scale random field using the non-Gaussian stochastic model and about 15 seconds to solve a $8 \times 3$ $\mu$m$^2$ rectangular plate, using a Python environment on a 2.1 GHz CPU. Although a few hundreds to a few thousands plate samples are required to compute a macro-scale property distribution, this step can also by parallelized in a efficient way on several processors as the plate samples are independent from each other. For comparison purpose, the direct resolution of a 3D finite element model with an explicit discretization of the grains and of the surface roughness requires several hours (for one sample), in a C++ environment on a 2.1 GHz CPU. Moreover it bears emphasis that for a given thickness and a given deposition temperature, the steps (i)-(iii) do not have to be recomputed for different plate geometries as the stochastic model can be reused directly. The computational time is thus reduced to the resolution of the different plate finite element discretization samples, step (iv).

## 6. CONCLUSIONS

Defining the probability density function of macro-scale properties of interest when considering micro-scale uncertainties is a challenging task as direct simulations of the fully modeled problem in the frame of a Monte-Carlo analysis remain a computational burden. The recourse to a stochastic multi-scale approach drastically reduces the computational time of such an analysis, and makes it possible.

Toward this end we have developed a stochastic multi-scale approach in the context of polycrystalline thin MEMS.

Rough stochastic volume elements (RSVEs) are first built from XRD, SEM, and AFM experimental measurement on poly-silicon structures.

The uncertainties due to roughness, along with the uncertainties from grains distribution and orientation, are then first propagated up to the meso-scale by using a second-order computational



*Prepared using* nmeauth.cls
DOI: 10.1002/nme

homogenization process performed on the RSVEs. Owing to the gradient-enhanced second-order computational homogenization, the bending behavior of the generated volume elements can be extracted at the meso-scale. The RSVEs are defined from XRD, SEM, and AFM experimental measurement on poly-silicon structures.

The extracted stochastic behavior of the meso-scale properties is then modeled by building a random field generator. This stochastic model is built using the spectral method combined to a non-Gaussian mapping, while the positive definite nature of the material properties is ensured by the introduction of an adequate lower bound.

Meso-scale random fields are then generated as material inputs for plate stochastic finite elements which allows studying in a probabilistic way the effects of the different sources of uncertainty and of the MEMS dimensions on the vibration behavior.

## A. POSITIVE-DEFINITENESS AND SYMMETRY OF $\boldsymbol{U}$

### *A.1. Symmetry*

The matrix $\boldsymbol{U}$ can be written as:

$$\boldsymbol{U}^{(ij)} = \frac{\partial \boldsymbol{\psi}^{\star(i)}_{\sigma_{\text{plate}}}}{\partial \boldsymbol{\chi}^{\star(j)}_{\varepsilon}} \,. \tag{86}$$

The stress vector $\boldsymbol{\psi}^{\star}_{\sigma_{\text{plate}}}$ can be obtained from the plate energy:

$$\boldsymbol{\psi}^{\star(i)}_{\sigma} = \frac{\partial W}{\partial \boldsymbol{\chi}^{\star(i)}_{\varepsilon}} \,. \tag{87}$$

Using Eq. (87) into (86) gives:

$$\boldsymbol{U}^{(ij)} = \frac{\partial W}{\partial \boldsymbol{\chi}^{\star(i)}_{\varepsilon} \partial \boldsymbol{\chi}^{\star(j)}_{\varepsilon}} \,, \tag{88}$$

thus ensuring the symmetry of $\boldsymbol{U}$.

### *A.2. Positive-definiteness*

The positive-definiteness of $\boldsymbol{U}$ can be proven based on the plate energy once again. The plate energy, which is strictly positive, is defined as:

$$W = \frac{1}{2} \boldsymbol{\psi}^{\star T}_{\sigma_{\text{plate}}} \boldsymbol{\chi}^{\star}_{\varepsilon} = \frac{1}{2} \boldsymbol{\chi}^{\star T}_{\varepsilon} \boldsymbol{U} \boldsymbol{\chi}^{\star}_{\varepsilon} \,, \tag{89}$$



*Prepared using* nmeauth.cls
DOI: 10.1002/nme

thus ensuring the positive-definiteness of $\boldsymbol{U}$.

## ACKNOWLEDGMENT

The research has been funded by the Walloon Region under the agreement no 1117477 (CT-INT 2011-11-14) and by the Romanian UEFISCDI Agency contract ERA-NET MNT no 7-063/2012 (20122015) in the context of the ERA-NET MNT framework.

IMT Bucharest would like to thank A.C. Cosmin for processing the Poly-silicon, R. Gavrila for AFM measurements, and A. Baracu for her technological support.

Computational resources have been provided by the supercomputing facilities of the Consortium des Équipements de Calcul Intensif en Fédération Wallonie Bruxelles (CÉCI) funded by the Fond de la Recherche Scientifique de Belgique (FRS-FNRS).

## REFERENCES

1. Lucas V, Golinval JC, Paquay S, Nguyen VD, Noels L, Wu L. A stochastic computational multiscale approach; application to MEMS resonators. *Computer Methods in Applied Mechanics and Engineering* 2015; **294**:141 – 167, doi:http://dx.doi.org/10.1016/j.cma.2015.05.019. URL http://www.sciencedirect.com/science/article/pii/S0045782515001929.
2. Ghanem R, Spanos P. *Stochastic Finite Elements: A Spectral Approach*. Springer Verlag, 1991.
3. Lemaitre O, Knio O. *Spectral methods for uncertainty quantification - with applications to computational fluid dynamics*. Springer, 2010.
4. Stefanou G. The stochastic finite element method: Past, present and future. *Computer Methods in Applied Mechanics and Engineering* 2009; **198**(912):1031 – 1051, doi:http://dx.doi.org/10.1016/j.cma.2008.11.007.
5. Lepage S. *Stochastic finite element method for the modeling of thermoelastic damping in micro-resonators*. Leloup, 2007.
6. Stefanou G, Papadrakakis M. Stochastic finite element analysis of shells with combined random material and geometric properties. *Computer Methods in Applied Mechanics and Engineering* 2004; **193**(1):139–160.
7. Shinozuka M, Deodatis G. Response variability of stochastic finite element systems. *Journal of Engineering Mechanics* 1988; **114**(3):499–519, doi:10.1061/(ASCE)0733-9399(1988)114:3(499).
8. Harada T, Shinozuka M. The scale of correlation for stochastic fields–technical report. *Department of Civil Engineering and Engineering Mechanics, Columbia University, New York, NY* 1986; .



*Prepared using* nmeauth.cls
DOI: 10.1002/nme

9. Castañeda P, Suquet P. Nonlinear composites. *Advances in Applied Mechanics*, *Advances in Applied Mechanics*, vol. 34, van der Giessen E, Wu TY (eds.). Elsevier, 1997; 171 – 302, doi:10.1016/S0065-2156(08)70321-1.
10. Doghri I, Ouaar A. Homogenization of two-phase elasto-plastic composite materials and structures: Study of tangent operators, cyclic plasticity and numerical algorithms. *International Journal of Solids and Structures* 2003; **40**(7):1681 – 1712, doi:10.1016/S0020-7683(03)00013-1.
11. Wu L, Noels L, Adam L, Doghri I. A combined incremental-secant mean-field homogenization scheme with per-phase residual strains for elasto-plastic composites. *International Journal of Plasticity* 2013; **51**:80 – 102, doi: 10.1016/j.ijplas.2013.06.006.
12. Ghosh S, Lee K, Moorthy S. Multiple scale analysis of heterogeneous elastic structures using homogenization theory and voronoi cell finite element method. *International Journal of Solids and Structures* 1995; **32**(1):27 – 62, doi:http://dx.doi.org/10.1016/0020-7683(94)00097-G.
13. Feyel F. Multiscale {FE2} elastoviscoplastic analysis of composite structures. *Computational Materials Science* 1999; **16**(14):344 – 354, doi:10.1016/S0927-0256(99)00077-4.
14. Michel J, Moulinec H, Suquet P. Effective properties of composite materials with periodic microstructure: a computational approach. *Computer Methods in Applied Mechanics and Engineering* 1999; **172**(1-4):109 – 143, doi:10.1016/S0045-7825(98)00227-8.
15. Feyel F, Chaboche JL. Fe2 multiscale approach for modelling the elastoviscoplastic behaviour of long fibre sic/ti composite materials. *Computer Methods in Applied Mechanics and Engineering* 2000; **183**(34):309 – 330, doi: 10.1016/S0045-7825(99)00224-8.
16. Miehe C, Koch A. Computational micro-to-macro transitions of discretized microstructures undergoing small strains. *Archive of Applied Mechanics* 2002; **72**(4-5):300–317, doi:10.1007/s00419-002-0212-2.
17. Kouznetsova V, Brekelmans WAM, Baaijens FPT. An approach to micro-macro modeling of heterogeneous materials. *Computational Mechanics* 2001; **27**(1):37–48, doi:10.1007/s004660000212.
18. Kaczmarczyk Ł, Pearce CJ, Bićanić N. Scale transition and enforcement of rve boundary conditions in second-order computational homogenization. *International Journal for Numerical Methods in Engineering* 2008; **74**(3):506–522.
19. Geers M, Kouznetsova V, Brekelmans W. Multi-scale computational homogenization: Trends and challenges. *Journal of Computational and Applied Mathematics* 2010; **234**(7):2175 – 2182, doi: http://dx.doi.org/10.1016/j.cam.2009.08.077.
20. Ostoja-Starzewski M. Material spatial randomness: From statistical to representative volume element. *Probabilistic Engineering Mechanics* 2006; **21**(2):112 – 132, doi:http://dx.doi.org/10.1016/j.probengmech.2005.07.007.
21. Kanit T, Forest S, Galliet I, Mounoury V, Jeulin D. Determination of the size of the representative volume element for random composites: statistical and numerical approach. *International Journal of Solids and Structures* 2003; **40**(13-14):3647–3679, doi:10.1016/S0020-7683(03)00143-4.
22. Hoang T, Guerich M, Yvonnet J. Determining the size of RVE for nonlinear random composites in an incremental computational homogenization framework. *Journal of Engineering Mechanics* 2015; :AcceptedURL `https://hal-upec-upem.archives-ouvertes.fr/hal-01228966`.




*Prepared using* nmeauth.cls
DOI: 10.1002/nme

23. Fish J, Wu W. A nonintrusive stochastic multiscale solver. *International Journal for Numerical Methods in Engineering* 2011; **88**(9):862–879, doi:10.1002/nme.3201.
24. Mariani S, Martini R, Ghisi A, Corigliano A, Simoni B. Monte carlo simulation of micro-cracking in polysilicon mems exposed to shocks. *International Journal of Fracture* 2011; **167**(1):83–101.
25. Gusella V, Cluni F. Random field and homogenization for masonry with nonperiodic microstructure. *Journal of Mechanics of Materials and Structures* 2006; **1**(2):357–386, doi:10.2140/jomms.2006.1.357.
26. Mariani S, Martini R, Ghisi A, Corigliano A, Beghi M. Overall elastic properties of polysilicon films: A statistical investigation of the effects of polycrystal morphology. *International Journal for Multiscale Computational Engineering* 2011; **9**(3).
27. Yin X, Chen W, To A, McVeigh C, Liu W. Statistical volume element method for predicting microstructureconstitutive property relations. *Computer Methods in Applied Mechanics and Engineering* 2008; **197**(43 - 44):3516 – 3529, doi:http://dx.doi.org/10.1016/j.cma.2008.01.008. Stochastic Modeling of Multiscale and Multiphysics Problems.
28. Liebscher A, Proppe C, Redenbach C, Schwarzer D. Uncertainty quantification for metal foam structures by means of image analysis. *Probabilistic Engineering Mechanics* 2012; **28**:143 – 151, doi:http://dx.doi.org/10.1016/j.probengmech.2011.08.015. URL http://www.sciencedirect.com/science/article/pii/S0266892011000701, computational Stochastic Mechanics {CSM6}.
29. Mulay S, Becker G, Vayrette R, Raskin JP, Pardoen T, Galceran M, Godet S, Noels L. Multiscale modelling framework for the fracture of thin brittle polycrystalline films: application to polysilicon. *Computational Mechanics* 2015; **55**:73–91, doi:10.1007/s00466-014-1083-4.
30. Stefanou G, Savvas D, Papadrakakis M. Stochastic finite element analysis of composite structures based on material microstructure. *Composite Structures* 2015; **132**:384 – 392, doi:http://dx.doi.org/10.1016/j.compstruct.2015.05.044. URL http://www.sciencedirect.com/science/article/pii/S0263822315004183.
31. Trovalusci P, De Bellis ML, Ostoja-Starzewski M, Murrali A. Particulate random composites homogenized as micropolar materials. *Meccanica* 2014; **49**(11):2719–2727.
32. Trovalusci P, Ostoja-Starzewski M, De Bellis ML, Murrali A. Scale-dependent homogenization of random composites as micropolar continua. *European Journal of Mechanics-A/Solids* 2015; **49**:396–407.
33. Ma J, Sahraee S, Wriggers P, De Lorenzis L. Stochastic multiscale homogenization analysis of heterogeneous materials under finite deformations with full uncertainty in the microstructure. *Computational Mechanics* 2015; :1–17.
34. Pivovarov D, Steinmann P. Modified sfem for computational homogenization of heterogeneous materials with microstructural geometric uncertainties. *Computational Mechanics* 2016; **57**(1):123–147.
35. Clément A, Soize C, Yvonnet J. Computational nonlinear stochastic homogenization using a nonconcurrent multiscale approach for hyperelastic heterogeneous microstructures analysis. *International Journal for Numerical*




*Prepared using* nmeauth.cls
DOI: 10.1002/nme

*Methods in Engineering* 2012; **91**(8):799–824, doi:10.1002/nme.4293.

36. Yin X, Lee S, Chen W, Liu WK, Horstemeyer MF. Efficient random field uncertainty propagation in design using multiscale analysis. *Journal of Mechanical Design* 2009; **131**(2), doi:http://dx.doi.org/10.1115/1.3042159.
37. Wu L, Lucas V, Nguyen VD, Golinval JC, Paquay S, Noels L. A stochastic multi-scale approach for the modeling of thermo-elastic damping in micro-resonators. *Computer Methods in Applied Mechanics and Engineering* 2016; **310**:802–839.
38. Zhou HW, Kharas B, Gouma P. Microstructure of thick polycrystalline silicon films for mems application. *Sensors and Actuators A: Physical* 2003; **104**(1):1–5.
39. Feyel F. A multilevel finite element method (fe2) to describe the response of highly non-linear structures using generalized continua. *Computer Methods in Applied Mechanics and Engineering* 2003; **192**(2830):3233 – 3244, doi:10.1016/S0045-7825(03)00348-7.
40. Kouznetsova V, Geers MG, Brekelmans WM. Multi-scale constitutive modelling of heterogeneous materials with a gradient-enhanced computational homogenization scheme. *International Journal for Numerical Methods in Engineering* 2002; **54**(8):1235–1260.
41. Coenen E, Kouznetsova V, Geers M. Computational homogenization for heterogeneous thin sheets. *International Journal for Numerical Methods in Engineering* 2010; **83**(8-9):1180–1205.
42. Cong Y, Nezamabadi S, Zahrouni H, Yvonnet J. Multiscale computational homogenization of heterogeneous shells at small strains with extensions to finite displacements and buckling. *International Journal for Numerical Methods in Engineering* 2015; **104**(4):235–259.
43. Baxter S, Graham L. Characterization of random composites using moving-window technique. *Journal of Engineering Mechanics* 2000; **126**(4):389–397, doi:10.1061/(ASCE)0733-9399(2000)126:4(389).
44. Cho H, Venturi D, Karniadakis G. Karhunenlove expansion for multi-correlated stochastic processes. *Probabilistic Engineering Mechanics* 2013; **34**(0):157 – 167, doi:http://dx.doi.org/10.1016/j.probengmech.2013.09.004.
45. Shinozuka M. Simulation of multivariate and multidimensional random processes. *The Journal of the Acoustical Society of America* 1971; **49**(1B):357–368, doi:http://dx.doi.org/10.1121/1.1912338.
46. Shinozuka M, Jan CM. Digital simulation of random processes and its applications. *Journal of Sound and Vibration* 1972; **25**(1):111 – 128, doi:http://dx.doi.org/10.1016/0022-460X(72)90600-1.
47. Popescu R, Deodatis G, Prevost J. Simulation of homogeneous nongaussian stochastic vector fields. *Probabilistic Engineering Mechanics* 1998; **13**(1):1 – 13, doi:10.1016/S0266-8920(97)00001-5.
48. Yamazaki F, Shinozuka M. Digital generation of non-gaussian stochastic fields. *Journal of Engineering Mechanics* 1988; **114**(7):1183–1197.
49. Deodatis G, Micaletti RC. Simulation of highly skewed non-gaussian stochastic processes. *Journal of engineering mechanics* 2001; **127**(12):1284–1295.
50. Das S, Ghanem R. A bounded random matrix approach for stochastic upscaling. *Multiscale Modeling & Simulation* 2009; **8**(1):296–325, doi:10.1137/090747713.



*Prepared using* nmeauth.cls
DOI: 10.1002/nme

51. Wells GN, Dung NT. A {C0} discontinuous galerkin formulation for kirchhoff plates. *Computer Methods in Applied Mechanics and Engineering* 2007; **196**(3536):3370 – 3380, doi:http://dx.doi.org/10.1016/j.cma.2007.03.008. URL http://www.sciencedirect.com/science/article/pii/S0045782507001429.
52. Noels L, Radovitzky R. A new discontinuous galerkin method for kirchhoff–love shells. *Computer Methods in Applied Mechanics and Engineering* 2008; **197**(33):2901–2929.
53. Der Kiureghian A, Ke J. The stochastic finite element method in structural reliability. *Probabilistic Engineering Mechanics* 1988; **3**(2):83 – 91, doi:http://dx.doi.org/10.1016/0266-8920(88)90019-7.
54. Becker G, Geuzaine C, Noels L. A one field full discontinuous galerkin method for kirchhofflove shells applied to fracture mechanics. *Computer Methods in Applied Mechanics and Engineering* 2011; **200**(45-46):3223 – 3241, doi:http://dx.doi.org/10.1016/j.cma.2011.07.008.
55. Kouznetsova V, Geers M, Brekelmans W. Multi-scale second-order computational homogenization of multi-phase materials: a nested finite element solution strategy. *Computer Methods in Applied Mechanics and Engineering* 2004; **193**(4851):5525 – 5550, doi:http://dx.doi.org/10.1016/j.cma.2003.12.073. URL http://www.sciencedirect.com/science/article/pii/S0045782504002853, advances in Computational Plasticity.
56. Nguyen VD, Becker G, Noels L. Multiscale computational homogenization methods with a gradient enhanced scheme based on the discontinuous galerkin formulation. *Computer Methods in Applied Mechanics and Engineering* 2013; **260**:63–77.
57. Soize C. Random matrix theory for modeling uncertainties in computational mechanics. *Computer Methods in Applied Mechanics and Engineering* 2005; **194**(12 - 16):1333 – 1366, doi: http://dx.doi.org/10.1016/j.cma.2004.06.038. Special Issue on Computational Methods in Stochastic Mechanics and Reliability Analysis.
58. Guilleminot J, Noshadravan A, Soize C, Ghanem R. A probabilistic model for bounded elasticity tensor random fields with application to polycrystalline microstructures. *Computer Methods in Applied Mechanics and Engineering* 2011; **200**(17 - 20):1637 – 1648, doi:http://dx.doi.org/10.1016/j.cma.2011.01.016.
59. Morris MC, McMurdie HF, Evans EH, Paretzkin B, de Groot JH, Hubbard SJ Camden R and-Carmel. Section 13. data for 58 substances. *Standard X-ray Diffraction Powder Patterns*, van der Giessen E, Wu TY (eds.). Technical Report Archive and Image Library, UNT Library, 1976. URL http://digital.library.unt.edu/ark:/67531/metadc13205/.
60. Geuzaine C, Remacle JF. Gmsh: A 3-d finite element mesh generator with built-in pre- and post-processing facilities. *International Journal for Numerical Methods in Engineering* 2009; **79**(11):1309–1331, doi: 10.1002/nme.2579.




*Prepared using* nmeauth.cls
DOI: 10.1002/nme